Taylor & Francis
Taylor & Francis Group

EFFECTS OF H_2O AND CO_2 DILUTION ON THE CATALYTIC AND GAS-PHASE COMBUSTION OF METHANE OVER PLATINUM AT ELEVATED PRESSURES

MICHAEL REINKE
JOHN MANTZARAS
ROLF BOMBACH
SABINE SCHENKER
NICLAS TYLLI

Paul Scherrer Institute, Combustion Research,
Villigen PSI, Switzerland

KONSTANTINOS BOULOUCHOS

Laboratory for Aerothermochemistry and Combustion
Systems, Swiss Federal Institute of Technology
Zurich (ETHZ), Zurich, Switzerland

The impact of large exhaust gas dilution (up to 59.5% H_2O and 30.3% CO_2 per vol.) on the heterogeneous (catalytic) and homogeneous (gas-phase) steady combustion of fuel-lean $CH_4/O_2/N_2$ mixtures over platinum has been investigated experimentally and numerically at pressures of 5 to 14 bar. In situ, one-dimensional Raman measurements of major gas-phase species concentrations and planar laser induced fluorescence (LIF) of the OH radical were used to assess the heterogeneous and homogeneous combustion processes, respectively. Comparisons between measurements and

553

predictions have yielded catalytic and gas-phase chemical reaction schemes suitable for the combustion of methane with large H_2O and CO_2 dilution. The addition of water inhibits the catalytic reactivity due to the increase in the surface coverage of OH(s) that, in turn, reduces the available free platinum sites. This inhibition has been quantified in terms of operating pressure, temperature, and amount of water dilution through an appropriate one-step catalytic reaction for the complete oxidation of methane. Water promotes chemically the onset of homogeneous ignition, as it directly impacts the radical pool buildup. On the other hand, the chemical effect of CO_2 on either reaction pathway is negligible. The influence of H_2O and CO_2 dilution to the coupling between the two reaction pathways is elucidated and implications for the application of catalytically stabilized combustion to new power generation cycles with large exhaust gas dilution are addressed.

INTRODUCTION

Catalytically stabilized thermal combustion (CST) provides the best available and most cost efficient low-NO_x combustion technology for gas turbines (Beebe et al., 2000; ONSE, 1999; Schlegel et al., 1996). In CST nearly half of the fuel is converted heterogeneously (catalytically) in Pd- and/or Pt-coated honeycomb reactors and the remaining is combusted in a follow-up homogeneous (gaseous) burnout zone (Beebe et al., 2000; Carroni et al., 2002). The standard CST involves fuel-lean catalytic and gaseous combustion of natural gas in air. In the last years, however, technologies for the efficient combustion of natural-gas and air (or pure oxygen) diluted with large amounts of recycled exhaust gas (H_2O and CO_2) have received increased attention. One such example is the advanced zero emissions power process (Griffin et al., 2004), which aims at mitigating both NO_x and CO_2 in power plants. Therein nitrogen is separated from air and natural gas is combusted at moderate temperatures (up to 1500 K) in a stream of oxygen and recycled exhaust gas with the latter comprising up to 90% vol. of the reactor feed. Combustion in pure oxygen rather than air circumvents the formation of NO_x. Moreover, the lack of N_2 allows for an easy separation of the non-recycled CO_2 from H_2O in the exhaust, thus facilitating the sequestration or

further disposal of CO_2. Pure gas-phase combustion of such heavily diluted mixtures at moderate temperatures is particularly challenging, rendering CST a viable alternative. Understanding the impact of large H_2O and CO_2 dilution on the catalytic and the low-temperature gaseous kinetics of CH_4 (the main constituent of natural gas) as well as on the coupling of the two pathways and further providing validated hetero-/homogeneous chemical reaction schemes are issues of prime interest for the advancement of new power generation cycles. The validated catalytic and gas-phase kinetics are indispensable input in numerical codes used for reactor design.

The assessment of the catalytic and gaseous reactivities at turbine-relevant conditions is a demanding task. To this direction, Appel et al. (2002) and Reinke et al. (2004) have recently introduced the methodology of in situ spatially-resolved Raman measurements of major gas-phase species concentrations over the catalyst as a direct means to assess, in conjunction with detailed numerical predictions, the catalytic reactivity at realistic operating conditions. The latter work (Reinke et al., 2004) demonstrated the validity of the heterogeneous reaction scheme of Deutschmann et al. (2000) for the complete oxidation of fuel-lean CH_4/air mixtures over polycrystalline platinum at $4 \, \text{bar} \leq p \leq 16 \, \text{bar}$, and further provided reduced catalytic schemes based on the validated mechanism. Appel et al. (2005a) extended the aforementioned methodology to the partial catalytic oxidation of fuel-rich CH_4/air mixtures to synthesis gas over rhodium at moderate pressures (6 bar). Spatially resolved measurements of species concentrations over a catalyst have also been reported in stagnation-flows: Sidwell et al. (2002, 2003) used micro-probe sampling to investigate the catalytic kinetics of methane over hexaaluminates at atmospheric pressure and Taylor et al. (2003) applied Raman spectroscopy to assess the performance of various catalytic schemes in the partial oxidation of methane over platinum at 40 mbar.

Although typical honeycomb catalytic reactors have sufficiently large surface-to-volume ratios in order to promote the heterogeneous fuel conversion, the impact of gas-phase chemistry cannot be always ignored at elevated pressures (Reinke et al., 2004). The preferred approach for the investigation of gaseous chemistry is to measure the concentration of a key radical (typically OH) above the catalyst with laser-induced fluorescence (LIF) (Cattolica and Schefer, 1983; Dogwiler et al., 1998; Griffin et al., 1989; Reinke et al., 2002). Furthermore, the

combination of Raman and LIF has provided a powerful tool for the assessment of both heterogeneous and homogeneous chemical pathways. Using OH LIF to monitor the onset of homogeneous ignition, Appel et al. (2002) investigated the gas-phase chemistry in fuel-lean H_2/air combustion over Pt at $p = 1$ bar. Dogwiler et al. (1998) and Reinke et al. (2002, 2005) carried out similar studies for fuel-lean CH_4/air combustion over Pt at $p = 1$ bar and 2.4 bar $\leq p \leq 16$ bar, respectively. In a comparative study of different gas-phase reaction schemes, it was demonstrated (Reinke et al., 2005) that the C1/H/O mechanism of Warnatz et al. (1996) reproduced the measured homogeneous ignition characteristics of CH_4 over Pt surfaces in the pressure range 6 bar $\leq p \leq 16$ bar.

To achieve good agreement over the entire range 1 bar $\leq p \leq 16$ bar (encompassing all catalytic heat and power generating systems, e.g. industrial boilers, microreactors and large gas-turbines), a modification in the scheme of Warnatz et al. (1996) has been proposed in Reinke et al. (2005). Based on the modified scheme, reduced homogeneous mechanisms have been constructed (Reinke et al., 2005), which are of particular interest in demanding CST reactor design computations. A first study of the impact of large H_2O and CO_2 dilution on the gaseous chemistry during catalytic combustion of methane over Pt was undertaken in Reinke et al. (2005a). Therein, the catalytic methane conversion was mass-transport-limited, hence only allowing for evaluation of the gaseous kinetics.

The impact of H_2O and CO_2 dilution on the heterogeneous reactivity of Pt catalysts as well as on the hetero-/homogeneous chemistry coupling has not hitherto been elaborated at turbine-relevant conditions. Previous works have investigated experimentally the effect of water on the Pd (Ciuparu and Pfefferle, 2001; Groppi et al., 2001; Ibashi et al., 2003; Kikuchi et al., 2002; van Giezen et al., 1999) and to a lesser extent on the Pt reactivity (Gelin et al., 2003; Urfels et al., 2004) during the complete oxidation of methane. The impact of CO_2 was also addressed in some of the Pd studies (Ibashi et al., 2003; van Giezen et al., 1999). The aforementioned works were limited to atmospheric pressure, substantially lower dilution (H_2O and CO_2 up to 20% and 5% vol., respectively) and lower temperatures (up to 850 K) compared to the requirements of CST-based turbine reactors. Moreover, the Pt studies (Gelin et al., 2003; Urfels et al., 2004) examined only the oxidation of CH_4 traces (~ 2000 ppmv). Finally, global measurements (exhaust gas

analysis) rather than in situ techniques have been applied in all the previous works.

The present study undertakes an experimental and numerical investigation of the catalytic combustion of fuel-lean CH_4/O_2 mixtures diluted with H_2O/N_2, CO_2/N_2 or H_2O/CO_2 (H_2O and CO_2 contents up to 59.5% and 30.3% vol., respectively) over polycrystalline Pt. Experiments have been performed in an optically accessible channel-flow catalytic reactor at steady and laminar operating conditions with pressures and surface temperatures spanning the ranges $5\,bar \leq p \leq 14\,bar$ and $825\,K \leq T \leq 1430\,K$. The concentrations of major gas-phase species and of the OH radical were assessed with one-dimensional Raman and planar LIF measurements, respectively. Simulations were carried out with an elliptic 2-D CFD code that included elementary hetero-/homogeneous chemical reaction schemes and detailed transport. The main objectives were to elucidate the impact of large H_2O and CO_2 addition on steady heterogeneous combustion and to assess the applicability of existing catalytic reaction schemes, to study the hetero-/homogeneous chemistry coupling and, finally, to further extend the previous work (Reinke et al., 2005a) on gas-phase combustion with exhaust gas dilution.

The test rig along with the measuring techniques and the computational model are introduced first. Comparisons between Raman measurements and numerical predictions lead to the validation of an elementary heterogeneous reaction scheme, which is further used to investigate the impact of H_2O and CO_2 on the catalytic reactivity. The coupling between the heterogeneous and homogenous pathways and the influence of CO_2 and H_2O on gas-phase combustion are finally discussed.

EXPERIMENTAL

High-Pressure Catalytic Reactor

The test rig consisted of a channel-flow catalytic reactor that formed a liner inside a high-pressure tank (Figure 1a, 1b), and a steam-generator supplying superheated steam (Figure 1c). The reactor/tank assembly has been used in earlier studies (Appel et al., 2002; Reinke et al., 2002, 2005) so that a brief description is given next. The reactor itself comprised two horizontal non-porous ceramic plates made of Si[SiC] (300 mm long,
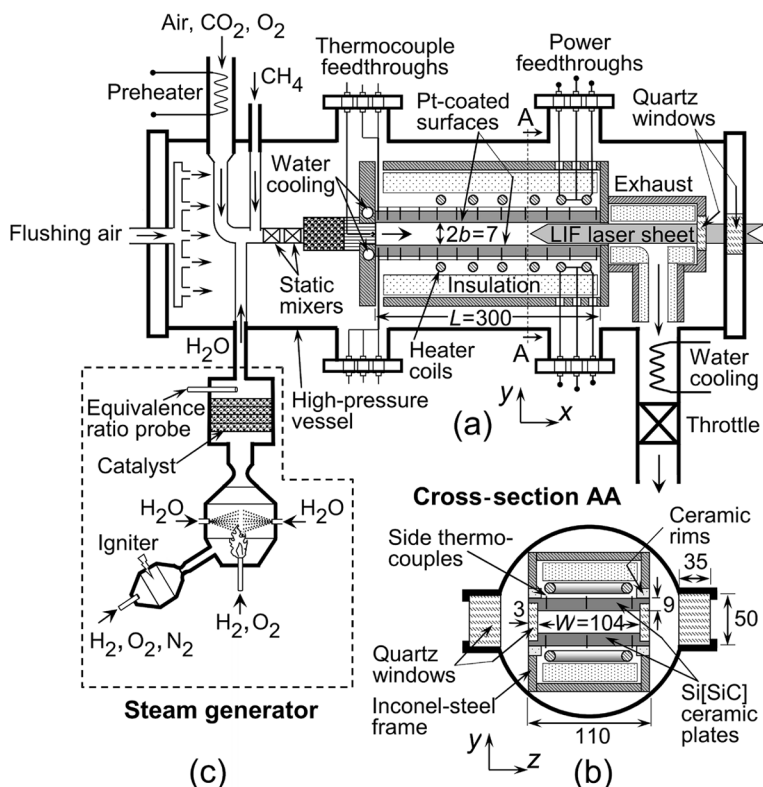
Figure 1. Schematic of the test rig: (a, b) high-pressure catalytic reactor, (c) steam-generator. All lengths are in mm.

110 mm wide, 9 mm thick, positioned 7 mm apart) and two vertical quartz glass windows (3 mm thick, 12 mm high and 300 mm long). The lateral window separation was 104 mm and the reactor volume was delineated by the $300 \times 104 \times 7 \, \text{mm}^3$ enclosure (Figure 1a, 1b). Both $300 \times 7 \, \text{mm}^2$ quartz glass sides provided optical access for laser-based measurements. A platinum coating was applied to the inner Si[SiC] surfaces with the procedure outlined in the forthcoming section on catalyst preparation. An insulating porous fiber ceramic material was positioned 20 mm above the outer Si[SiC] surfaces. Finally, the reactor was mounted inside an inconel-steel frame with the support of ceramic rims.

The temperature of each catalytic plate was measured with twelve S-type (Pt-10%Rh/Pt) thermocouples arranged along the *x-y* symmetry

plane (Figure 1a). The thermocouples were embedded 0.9 mm beneath the Pt coating, through 1.2-mm in diameter and 8.1-mm deep holes eroded from the uncoated outer Si[SiC] surfaces. Side thermocouples were also placed at $x = 22$ and 110 mm and $z = \pm 40$ mm. Two adjustable-power resistive heating coils, extending over the length $100\,\text{mm} \leq x \leq 300\,\text{mm}$, were positioned 15 mm above each ceramic plate. External heating was particularly important in achieving the high surface temperatures required for homogeneous ignition. On the other hand, the catalytic reactivity studies required lower surface temperatures in order to attain kinetically controlled fuel conversion away from the mass transport limit. This was accomplished by reducing the electric power of the heaters and—when necessary—by additional water cooling of the inconel steel frame that was in direct contact with the $9 \times 110\,\text{mm}^2$ front faces of the ceramic plates (Figure 1a).

An oil-free compressor provided dry air and high-pressure bottles supplied technical-grade CH_4 ($> 99.5\%$), O_2 and CO_2. Pure O_2 was used in addition to the air supply so as to control the amount of N_2 dilution. All flows were regulated and measured by Brooks mass-flow controllers that yielded equivalence ratio accuracies better than $\pm 0.5\%$. The air/O_2/CO_2 flows were preheated by a 3-kW electric heater to temperatures up to $450°C$ and then mixed with superheated steam (see Figure 1a) produced by a dedicated steam-generator. Room-temperature methane was injected farther downstream and the resulting CH_4/air/O_2/CO_2/H_2O mixture passed through two sequential static mixers (Sulzer SMV), a 40-mm-long packing of ceramic spheres (2 mm in diameter) and a 40-mm-long inert ceramic honeycomb structure to straighten the flow. A thermocouple placed inside one channel of the inert honeycomb monitored the inlet temperature of the reactor. Finally, an inconel steel exhaust section insulated with a porous fiber ceramic directed the combustion products towards a water-cooled outlet of the high-pressure tank.

The high-pressure vessel that housed the reactor was a stainless steel structure with a length of 1.8 m and an internal diameter of 0.28 m. The vessel was equipped with two 350-mm long and 35-mm thick quartz glass windows, which sustained pressures up to 20 bar and maintained optical accessibility from both reactor sides (Figure 1b). Two additional quartz windows (one located at the reactor exhaust and the other at the rear flange of the vessel, see Figure 1a) provided a streamwise optical access for the LIF excitation beam. A continuous flow of flushing air

removed any unwanted combustion products from the free volume between the vessel and the reactor assembly. Finally, the thermocouple and heater power lines were driven inside the reactor through high-pressure feedthroughs positioned on four dedicated flanges of the vessel.

Steam Generator

The steam generator (Figure 1c) was a new addition to the test rig and could produce superheated steam at flow rates of 0.9–20 g/s, pressures up to 30 bar and temperatures of 200–1000°C. Since such high mass flow rates could not be supplied by common electric-heater-based systems, the heat of H_2/O_2 combustion was used to vaporize known amounts of liquid water. The device consisted of a combustion chamber, a gas/water supply and an electronic control unit. The combustion chamber, which was designed by DLR (Beer and Willms, 1993), comprised three modules: the hot gas igniter, the main combustion chamber and the catalytic converter. In the hot gas igniter, an $H_2/O_2/N_2$ mixture (the N_2 was added for safety reasons) was ignited by conventional spark plugs. The generated hot exhaust gases were flushed into the main combustion chamber to ignite a central H_2/O_2 flame, which was stabilized by the recirculation zone of a sudden geometric expansion. A continuous spray injection of demineralized liquid water controlled the amount of steam and the combustion temperature. A follow-up catalytic module consisting of a Ni-Pd catalyst packing converted any escaping H_2 and O_2 to H_2O (Figure 1c). In practice, the central H_2/O_2 burner was operated slightly fuel-lean ($0.98 \leq \varphi < 1$) in order to avoid hydrogen breakthrough that could potentially affect the measurements in the channel-reactor. An equivalence-ratio probe (similar to that used in automotive engines) positioned at the downstream end of the catalytic converter monitored the O_2 content and determined the degree of steam purity.

The gaseous flows in the igniter were regulated by needle valves. Step-motor-controlled needle valves regulated the liquid water and the gaseous flows of the main combustor; the liquid water flow was measured with a Micro-Motion-Elite sensor and the gaseous mass flows with Brooks meters. A thermocouple located at the end of the catalytic converter monitored the steam temperature. Both the vaporized liquid water and the H_2O combustion product were accounted for in the total amount of produced steam.

Catalyst Preparation

The inner Si[SiC] surfaces were coated with Pt using plasma vapor deposition (PVD). A 1.5-μm thick nonporous Al$_2$O$_3$ layer was deposited first, followed by a 2.2-μm-thick Pt layer. The Al$_2$O$_3$ layer served as a barrier to Si-Pt interactions. The thick Pt coating on top of the non-porous Al$_2$O$_3$ layer closely resembled a polycrystalline Pt surface and this was verified with independent surface area and surface composition measurements. The total and active surface areas were measured with BET (Kr-physisorption) and CO-chemisorption, respectively. The BET verified the absence of surface porosity whereas both BET and CO-chemisorption revealed the same total and active areas (0.26 m^2/grCat), suggesting that the surface was covered only with Pt. The latter was also verified with independent X-ray Photoelectron Spectroscopy (XPS) surface composition measurements before and after the Raman/LIF experiments: the XPS analyses have shown that bulk Al or Si did not diffuse on the surface even after extended periods of reactor operation. The surface site density of polycrystalline Pt (2.7×10^{-9} mol/cm^2 (Deutschmann et al., 1996)) was, therefore, used in the numerical model.

Laser Diagnostics

The planar OH-LIF and 1-D Raman set-up is depicted in Figure 2. For the LIF experiment, the 532-nm second harmonic radiation of a pulsed Nd:YAG laser (Quantel YG781C20) pumped a tunable dye laser (Quantel TDL50). The dye output was frequency-doubled to 285 nm to excite the $A(v=1) \leftarrow X(v'=0)$ transition of the OH radical. A cylindrical lens telescope and a 1-mm slit mask transformed the 285 nm beam into a thin laser sheet that propagated counterflow along the x-y symmetry plane (see Figures 1a and 2). The fluorescence of both $(1-1)$ and $(0-0)$ transitions at 308 and 314 nm, respectively, was collected by an intensified CCD camera (LaVision FlameStar 2F, 576×384 pixels) through one pair of reactor and tank side windows. Individual channel areas of 120×7 mm^2 were imaged on a 576×34 pixel area and the camera was traversed axially to map the entire reactor extent. At each particular position, four hundred single-shot LIF images were averaged to increase the signal-to-noise ratio. The LIF signal was calibrated with absorption measurements: therein, the laser beam crossed the reactor laterally (z) through all four side quartz windows, as also done in earlier studies (Appel et al., 2002; Dogwiler et al., 1998; Reinke et al., 2002).
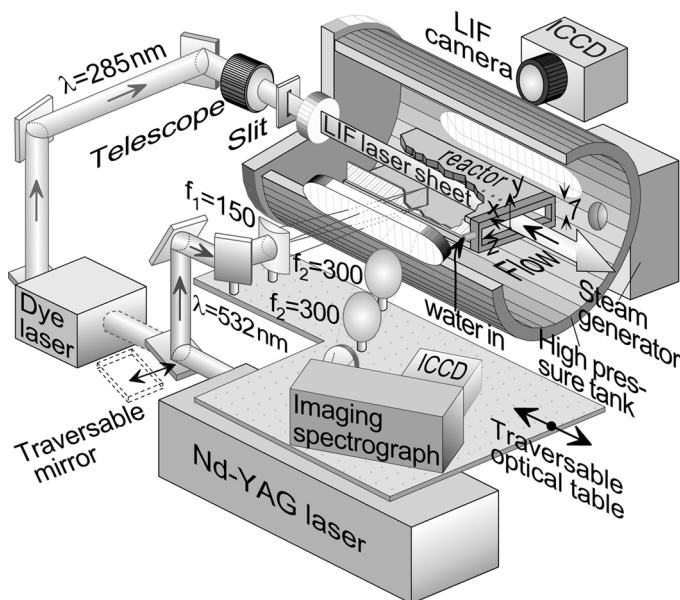
Figure 2. Optical setup for the Raman and OH LIF. All focal lengths are in mm.

The second harmonic radiation of the Nd:YAG laser also provided the excitation source for the spontaneous Raman measurements. A traversable mirror directed the 532-nm beam either to the Raman or to the dye-laser/LIF set-up (Figure 2). Simultaneous acquisition of both Raman and LIF data was not necessary, given the steady and laminar operating conditions. The LIF data were acquired at regular time intervals in-between the Raman measurements. An $f_1 = 150$ mm cylindrical lens focused the 532 nm beam, through the second pair of side quartz windows, to a ~ 0.3 mm thick vertical line inside the reactor (Figure 2). The focal line spanned the entire 7-mm-high transverse plate separation. To increase the light collection angle and to minimize thermal beam steering, the focal line was laterally offset from the x-y symmetry plane ($z = 15$ mm) (Appel et al., 2002; Reinke et al., 2004). The Raman-scattered light was collected at $50°$ with respect to the sending optical path and was focused by two $f_2 = 300$ mm spherical lenses on the entrance slit of a 25-cm imaging spectrograph (Chromex 250i). The spectrograph was equipped with an intensified CCD camera identical to that of the LIF setup; 2000 images were averaged to improve

the signal-to-noise ratio. The 576×384 pixel dimensions of the CCD camera corresponded to wavelength and transverse distance, respectively. The 7 mm channel gap was resolved with 250 pixels that were further binned to 63 pixels, resulting in a spatial resolution of 0.1 mm.

The effective Raman cross-sections, which included transmission efficiencies, were evaluated by recording the signals of pure CH$_4$, air, and completely burned gases of known composition. Spectroscopic coefficients for the Raman cross-section of CH$_4$ and H$_2$O were taken from Steiner (2002) und Eisenberg (1995), respectively. For the diatomic species, theoretical harmonic oscillator cross-section variations were considered (Brockhinke et al., 1995). Both sending and collecting Raman optics were mounted on an axially-traversable optical table (Figure 2), which allowed measurements over the length $12\,\text{mm} \leq x \leq 163\,\text{mm}$. Raman measurements closer than 0.6 mm to both catalytic walls were discarded due to low signal-to-noise ratio. Details of the Raman and the OH LIF experiments have been provided elsewhere (Appel et al., 2002; Dogwiler et al., 1998; Reinke et al., 2004). The measurement accuracy will be discussed in the Results section.

Operating Conditions

The investigated conditions (shown in Table 1) spanned the pressure range $5\,\text{bar} \leq p \leq 14\,\text{bar}$. The Reynolds numbers of Table 1 were based on the uniform inlet properties and the channel hydraulic diameter ($=13.1$ mm) and were kept below 2200 except in Cases 1 and 3. Since those two cases had the lowest H$_2$O dilution, an increased total reactor mass throughput was necessary (Re$_{\text{IN}}$ up to 3700) to cope with the minimum mass-flow requirements of the steam generator. Nonetheless, Cases 1 and 3 could still be treated with a laminar model since the strong flow laminarization (caused by the increase in the viscosity due to the heat transfer from the hot catalytic plates) guaranteed laminar flow conditions even at considerably higher incoming Reynolds numbers (Appel et al., 2005). The dilution comprised either H$_2$O/N$_2$ or CO$_2$/N$_2$ except in Cases 8 and 9 (H$_2$O/CO$_2$). To avoid excessive surface temperatures that could endanger the catalyst integrity, the fuel-to-oxygen equivalence ratio was set to $\phi = 0.40$ (0.50 for the H$_2$O/CO$_2$ dilution). For the catalytic reactivity studies, the relevant measurements were those of Cases 1 to 9 that exhibited kinetically controlled heterogeneous methane conversion. Cases 10 to 14 displayed mass-transport-limited catalytic

Table 1. Experimental conditions[a]

Case	p (bar)	% CH$_4$	% O$_2$	% H$_2$O	% CO$_2$	% N$_2$	ϕ	U_{IN} (m/s)	T_{IN} (K)	Re$_{IN}$
1	5	4.5	22.6	24.2	0.0	48.7	0.40	3.03	605	3034
2	5	4.3	21.7	51.8	0.0	22.2	0.40	1.85	618	2070
3	10	4.5	22.4	25.0	0.0	48.1	0.40	1.50	590	3744
4	10	4.5	22.4	49.7	0.0	23.4	0.40	0.83	576	2115
5	14	4.6	23.2	48.4	0.0	23.8	0.40	0.59	586	2029
6	5	4.5	22.3	0.0	10.2	63.0	0.40	1.19	581	1687
7	14	5.0	24.9	0.0	30.3	39.8	0.40	0.41	576	1856
8	5	4.5	18.0	52.1	25.4	0.0	0.50	1.58	602	2189
9	14	4.6	18.6	50.2	26.6	0.0	0.50	0.54	598	2133
10	12	4.5	22.7	59.5	0.0	13.3	0.40	0.51	580	1513
11	14	4.8	24.1	57.1	0.0	14.0	0.40	0.39	558	1477
12	5	4.9	24.8	0.0	30.3	40.0	0.40	0.72	616	1022
13	10	4.9	24.8	0.0	30.3	40.0	0.40	0.35	602	1038
14	14	4.9	24.8	0.0	30.3	40.0	0.40	0.25	598	1044

[a]pressure, % volumetric composition, equivalence ratio, inlet velocity, inlet temperature, and inlet Reynolds number. Homogeneous ignition is attained in Cases 10 to 14.

conversion due to the associated higher surface temperatures; however, the achieved homogeneous ignition rendered those cases suitable for the investigation of the gaseous pathway.

NUMERICAL

Two-Dimensional Channel Model

The governing equations for a 2-D, steady, elliptic laminar flow with heterogeneous and homogeneous chemical reactions were:

Continuity equation:

$$\frac{\partial(\rho u)}{\partial x} + \frac{\partial(\rho v)}{\partial y} = 0 \tag{1}$$

Momentum equations:

$$\frac{\partial(\rho uu)}{\partial x} + \frac{\partial(\rho vu)}{\partial y} + \frac{\partial p}{\partial x} - \frac{\partial}{\partial x}\left[2\mu\frac{\partial u}{\partial x} - \frac{2}{3}\mu\left(\frac{\partial u}{\partial x} + \frac{\partial v}{\partial y}\right)\right]$$
$$- \frac{\partial}{\partial y}\left[\mu\left(\frac{\partial u}{\partial y} + \frac{\partial v}{\partial x}\right)\right] = 0 \tag{2}$$

$$\frac{\partial(\rho uv)}{\partial x} + \frac{\partial(\rho vv)}{\partial y} + \frac{\partial p}{\partial y} - \frac{\partial}{\partial x}\left[\mu\left(\frac{\partial v}{\partial x} + \frac{\partial u}{\partial y}\right)\right]$$
$$- \frac{\partial}{\partial y}\left[2\mu\frac{\partial v}{\partial y} - \frac{2}{3}\mu\left(\frac{\partial u}{\partial x} + \frac{\partial v}{\partial y}\right)\right] = 0 \qquad (3)$$

Energy equation:

$$\frac{\partial(\rho uh)}{\partial x} + \frac{\partial(\rho vh)}{\partial y} + \frac{\partial}{\partial x}\left(\rho\sum_{k=1}^{Kg} Y_k h_k V_{k,x} - \lambda\frac{\partial T}{\partial x}\right)$$
$$+ \frac{\partial}{\partial y}\left(\rho\sum_{k=1}^{Kg} Y_k h_k V_{k,y} - \lambda\frac{\partial T}{\partial y}\right) = 0 \qquad (4)$$

Gas-phase species equations:

$$\frac{\partial(\rho u Y_k)}{\partial x} + \frac{\partial(\rho v Y_k)}{\partial y} + \frac{\partial}{\partial x}\left(\rho Y_k V_{k,x}\right) + \frac{\partial}{\partial y}\left(\rho Y_k V_{k,y}\right) - \dot{\omega}_k W_k = 0,$$
$$k = 1, \ldots, K_g \qquad (5)$$

Surface species coverage equations:

$$\frac{\partial\theta_m}{\partial t} = \sigma_m\frac{\dot{s}_m}{\Gamma}, \quad m = 1, \ldots, M_s \qquad (6)$$

Only the steady-state solutions of Eqs. (6) were of interest. Buoyancy was insignificant for the relatively high Reynolds numbers of Table 1 and the narrow vertical channel gap (7 mm).

The diffusion velocities in Eqs. (5) were computed using mixture average diffusion, including thermal diffusion for the light species H and H$_2$ (Kee et al., 1996):

$$\vec{V}_k = -(D_{km}/Y_k)\nabla Y_k + (D_k^T/\rho Y_k T)\nabla T, \quad k = 1, \ldots, K_g \qquad (7)$$

The system of equations was closed by the ideal gas and caloric state laws:

$$p = \frac{\rho RT}{\overline{W}} \text{ and } h_k = h_k^o(T_o) + \int_{T_o}^{T} c_{p,k} dT, \quad k = 1, \ldots, K_g \qquad (8)$$

The interfacial ($y=0$ and $y=2b$) boundary conditions were:

$$\left(\rho Y_k V_{k,y}\right)_{y=0} = W_k(\dot{s}_k)_{y=0} \quad -\left(\rho Y_k V_{k,y}\right)_{y=2b} = W_k(\dot{s}_k)_{y=2b} \qquad (9)$$

and

$$T(x, y = 0) = T_{W,L}(x), \ \ T(x, y = 2b) = T_{W,U}(x) \qquad (10)$$

with $T_{W,U}(x)$ and $T_{W,L}(x)$ the thermocouple-measured temperature distributions of the upper and lower wall, respectively. No-slip was applied for both velocity components at the gas-wall interfaces. The inlet conditions were uniform profiles for the temperature T_{IN} (measured), the axial velocity U_{IN} (deduced from the inlet temperature and the measured mass flow rates) and the species mass fractions $Y_{k,IN}$. At the outflow ($x = 300$ mm) the applied conditions were $v = 0$ and zero-Neumann for all other scalars. The governing equations were discretized with a finite volume scheme and the solution was obtained iteratively using a SIMPLER (Patankar, 1980) method for the pressure-velocity field. Details on the solution algorithm have been provided elsewhere (Dogwiler et al., 1999; Mantzaras et al., 2000). An orthogonal staggered grid of 380×120 points (in x and y, respectively) with finer x-spacing closer to the entrance and y-spacing closer to the walls was sufficient to produce a grid-independent solution.

In addition to the full elliptic model, an efficient 2-D parabolic model (Mantzaras et al., 2000a) was also used for the computationally intensive sensitivity analyses. The adequacy of the parabolic model has been demonstrated in pure catalytic combustion for inlet Reynolds numbers as low as 20 (Raja et al., 2000). In the presence of homogeneous ignition the applicability of the parabolic model was maintained by the magnitude of the inlet velocity (U_{IN}) and laminar flame speed (S_L): large U_{IN} and small S_L suppressed the upstream diffusion and rendered the parabolic approach valid (Mantzaras et al., 2000a). The low S_L of the present investigation (due to the fuel-lean incoming mixtures, high exhaust gas dilution and the negative pressure dependence $S_{L,CH4} \sim p^{-0.5}$) resulted in parabolic model predictions in good agreement with those of the full elliptic model.

Ideal Reactor Modeling

Ideal reactor computations were also used to investigate the underlying chemical processes. The surface perfectly stirred reactor (SPSR) package of CHEMKIN (Moffat et al., 1993) was employed. The SPSR governing equations were:

Gas-phase species equations:

$$-(1/\tau)(Y_k - Y_{k,\text{IN}}) + (1/\rho)[\dot{\omega}_k W_k + (S/V)\dot{s}_k W_k] = 0 \quad k = 1, \ldots, K_g \tag{11}$$

Energy equation:

$$
\begin{aligned}
& -(1/\tau) \sum_{k=1}^{K_g} Y_{k,\text{IN}}(h_k - h_{k,\text{IN}}) - (1/\rho) \\
& \times \left[\sum_{k=1}^{K_g} h_k \dot{\omega}_k W_k + (S/V) \sum_{k=1}^{K_g + M_s} h_k \dot{s}_k W_k \right] = 0
\end{aligned}
\tag{12}
$$

with τ, S and V the reactor residence time, surface, and volume, respectively. The surface coverage equations were provided by Eqs. (6) and the ideal gas laws by Eqs. (8).

Ignition delay times of pure gaseous mixtures were also computed in a constant pressure batch reactor using the SENKIN package (Lutz et al., 1996). The governing equations were:

Gas-phase species equation:

$$\frac{dY_k}{dt} = \frac{1}{\rho} \dot{\omega}_k W_k \quad k = 1, \ldots, K_g \tag{13}$$

Energy equation:

$$c_p \frac{dT}{dt} - \frac{1}{\rho} \sum_{k=1}^{K_g} h_k \dot{\omega}_k W_k = 0 \tag{14}$$

The set of Eqs. (13) and (14), supplemented by the gas laws of Eqs. (8), was solved subject to appropriate initial conditions.

Chemical Kinetics

The elementary heterogeneous scheme of Deutschmann et al. (2000) was used for the complete oxidation of CH$_4$ over Pt. This scheme has been validated in combustion of CH$_4$/air mixtures without exhaust gas dilution, over the following parameter ranges: $1\,\text{bar} \leq p \leq 16\,\text{bar}$, $0.31 \leq \varphi \leq 0.40$ and $780\,\text{K} \leq T \leq 1250\,\text{K}$ (Dogwiler et al., 1998; Reinke et al., 2004). Its applicability under high exhaust gas dilution will be examined herein. To facilitate the ensuing discussion, the catalytic scheme is provided in Table 2. The surface site density of polycrystalline

Table 2. Catalytic reaction scheme for methane oxidation on Pt[a]

Adsorption reactions	$A\ (\gamma)$	b	E
S1. $CH_4 + 2Pt(s) \rightarrow CH_3(s) + H(s)$	0.01	0.0	0.0
S2. $O_2 + 2Pt(s) \rightarrow 2O(s)$	0.023	0.0	0.0
S3. $O_2 + 2Pt(s) \rightarrow 2O(s)$	4.9×10^{12}	-0.5	0.0
S4. $H_2 + 2Pt(s) \rightarrow 2H(s)$	0.046	0.0	0.0
S5. $H + Pt(s) \rightarrow H(s)$	1.0	0.0	0.0
S6. $O + Pt(s) \rightarrow O(s)$	1.0	0.0	0.0
S7. $H_2O + Pt(s) \rightarrow H_2O(s)$	0.75	0.0	0.0
S8. $OH + Pt(s) \rightarrow OH(s)$	1.0	0.0	0.0
S9. $CO + Pt(s) \rightarrow CO(s)$	0.84	0.0	0.0
Surface reactions			
S10. $H(s) + O(s) = OH(s) + Pt(s)$	1.0×10^{13}	0.0	11.5
S11. $H(s) + OH(s) = H_2O(s) + Pt(s)$	1.0×10^{13}	0.0	17.4
S12. $OH(s) + OH(s) = H_2O(s) + O(s)$	1.0×10^{13}	0.0	48.2
S13. $C(s) + O(s) \rightarrow CO(s) + Pt(s)$	1.0×10^{13}	0.0	62.8
S14. $CO(s) + Pt(s) \rightarrow C(s) + O(s)$	2.7×10^{9}	0.0	184.0
S15. $CO(s) + O(s) \rightarrow CO_2(s) + Pt(s)$	1.0×10^{13}	0.0	105.0
S16. $CH_3(s) + Pt(s) \rightarrow CH_2(s)s + H(s)$	1.0×10^{13}	0.0	20.0
S17. $CH_2(s)s + Pt(s) \rightarrow CH(s) + H(s)$	1.0×10^{13}	0.0	20.0
S18. $CH(s) + Pt(s) \rightarrow C(s) + H(s)$	1.0×10^{13}	0.0	20.0
Desorption reactions			
S19. $2O(s) \rightarrow O_2 + 2Pt(s)$	1.0×10^{13}	0.0	213.2-60 θ_O
S20. $2H(s) \rightarrow H_2 + 2Pt(s)$	1.0×10^{13}	0.0	67.4-6 θ_H
S21. $H_2O(s) \rightarrow H_2O + Pt(s)$	1.0×10^{13}	0.0	40.3
S22. $OH(s) \rightarrow OH + Pt(s)$	1.0×10^{13}	0.0	192.8
S23. $CO_2(s) \rightarrow CO_2 + Pt(s)$	1.0×10^{13}	0.0	20.5
S24. $CO(s) \rightarrow CO + Pt(s)$	1.0×10^{13}	0.0	125.5

[a]From Deutschmann et al. (2000). In the surface and desorption reactions, the reaction rate coefficient is $k = AT^b \exp(-E/RT)$, $A(\text{sec}^{-1})$ and E (kJ/mol). In all adsorption reactions, except S3, A denotes a sticking coefficient (γ). Reactions S2 and S3 are duplicate. Reactions S1, S4 and S14 have a Pt-order of 2.3, 1 and 2, respectively. The suffix (s) denotes a surface species.

Pt ($\Gamma = 2.7 \times 10^{-9}\,\text{mol/cm}^2$) was used in the numerical predictions, as discussed in the catalyst preparation section. Surface thermochemical data for the reversible reactions S10-S12 of Table 2 were provided by Warnatz et al. (1994).

For gas-phase chemistry, the C1/H/O mechanism of Warnatz et al. (1996) was employed (25 species, 81 reversible and 27 irreversible reactions, including appropriate pressure dependencies for the reactions

CH$_3$ + H=CH$_4$, CH$_3$ + CH$_3$=C$_2$H$_6$ and CH$_3$OH=CH$_3$ + OH). The part of the C2 chemistry that led to recombination of C1 radicals to C2 species was also included in the mechanism, since previous CH$_4$/air studies (Reinke et al., 2005) have shown its importance even at the low equivalence ratios of catalytic combustion systems. The aptness of the aforementioned mechanism has been demonstrated for $p > 4$ bar, $900 \, \text{K} \leq T \leq 1400 \, \text{K}$ and $0.05 \leq \varphi \leq 0.50$ (Reinke et al., 2005). To reproduce the measurements at the lower pressure range $1 \, \text{bar} \leq p \leq 4 \, \text{bar}$, however, a correction in the kinetic parameters of the chain branching step CHO + M=CO + H + M was introduced (Reinke et al., 2005), which was additionally supported by recent kinetic measurements (Friedrichs et al., 2002). The modified scheme was applicable over the entire pressure range $1 \, \text{bar} \leq p \leq 16 \, \text{bar}$. Nonetheless, since the present investigation referred to $p \geq 5 \, \text{bar}$, the unaltered scheme of Warnatz was used (it provided practically the same results as the modified scheme). The thermodynamic database was included in the provided mechanism (Warnatz et al., 1996). The species diffusivities as well as the mixture viscosities and thermal conductivities were calculated using the CHEMKIN database (Kee et al., 1996). Gas-phase and surface reaction rates were evaluated using CHEMKIN (Kee et al., 1996a) and Surface-CHEMKIN (Coltrin et al., 1996), respectively. Finally, the prefixes S and R will denote a surface and a gaseous reaction, respectively.

RESULTS AND DISCUSSION, HETEROGENEOUS COMBUSTION

Comparisons Between Raman Measurements and Predictions

To assess the catalytic reactivity from the Raman measurements, it is first necessary to delineate the reactor extent with negligible gas-phase contribution. Streamwise profiles of the catalytic (C) and gaseous (G) methane conversions are provided in Figure 3 for three selected cases of Table 1. The profiles were calculated using the catalytic and gas-phase schemes of Deutschmann et al. (2000) and Warnatz et al. (1996), respectively; the validity of the latter will be discussed in the subsequent section on homogeneous combustion. The G profiles of Figure 3 were constructed by integrating the local volumetric gaseous reaction rates across the 7-mm transverse channel distance so as to facilitate comparisons with the catalytic surface rates; the latter referred to the
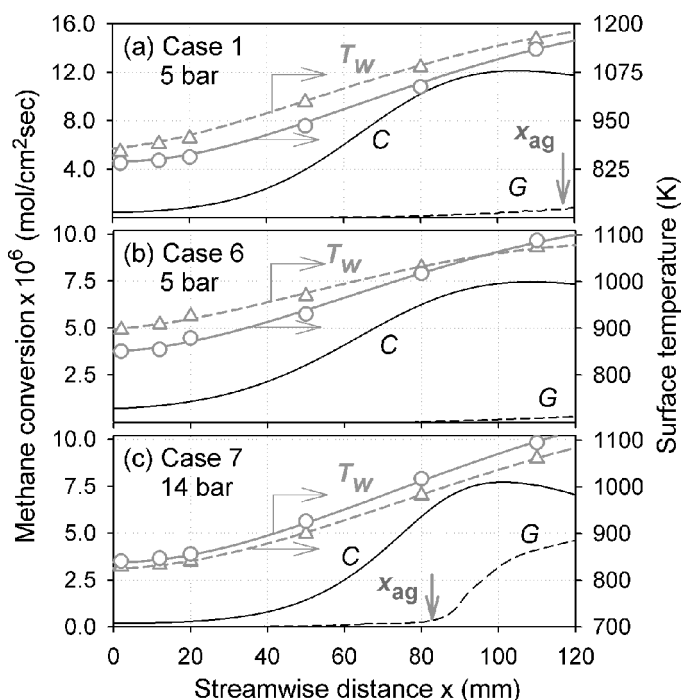
Figure 3. Computed streamwise profiles of catalytic (*C*, solid lines) and gaseous (*G*, dashed lines) methane conversions for three cases of Table 1. The onset of appreciable gaseous conversion is identified by the arrows marked x_{ag}. The symbols provide the measured surface temperatures and the gray lines are fits through the measurements: upper plate (circles, gray solid lines), lower plate (triangles, gray dashed lines).

combined contribution of the upper and lower catalytic walls. The onset of appreciable gas-phase contribution (defined as the position where the gaseous conversion amounted to 5% of the catalytic conversion) is designated in Figure 3 by the vertical arrows marked x_{ag}. Upstream of those locations the computations were practically unaffected by the inclusion of gas-phase chemistry, such that the reactor extent $0 < x \leq x_{ag}$ was suitable for catalytic reactivity studies. As evidenced in Figure 3, the contribution of the gaseous pathway was more pronounced at elevated pressures. It is clarified that the onset of appreciable gas-phase methane conversion did not imply the onset of homogeneous ignition: the OH LIF experiments have, after all, verified the absence of a flame for all Cases 1 to 9. As will be elaborated in the forthcoming homogeneous

combustion section, appreciable gas-phase methane conversion could still occur without an accompanying significant exothermicity.

Measured and predicted transverse profiles of CH_4, O_2, CO_2 and H_2O mole fractions are provided in Figure 4 (H_2O/N_2 dilution) and in Figure 5 (CO_2/N_2 or H_2O/CO_2 dilution). All profiles in Figures 4 and 5 pertained to axial positions $x \leq x_{ag}$, and for reasons of clarity only 30 out of the 63 transverse Raman points are shown. The profiles (measured
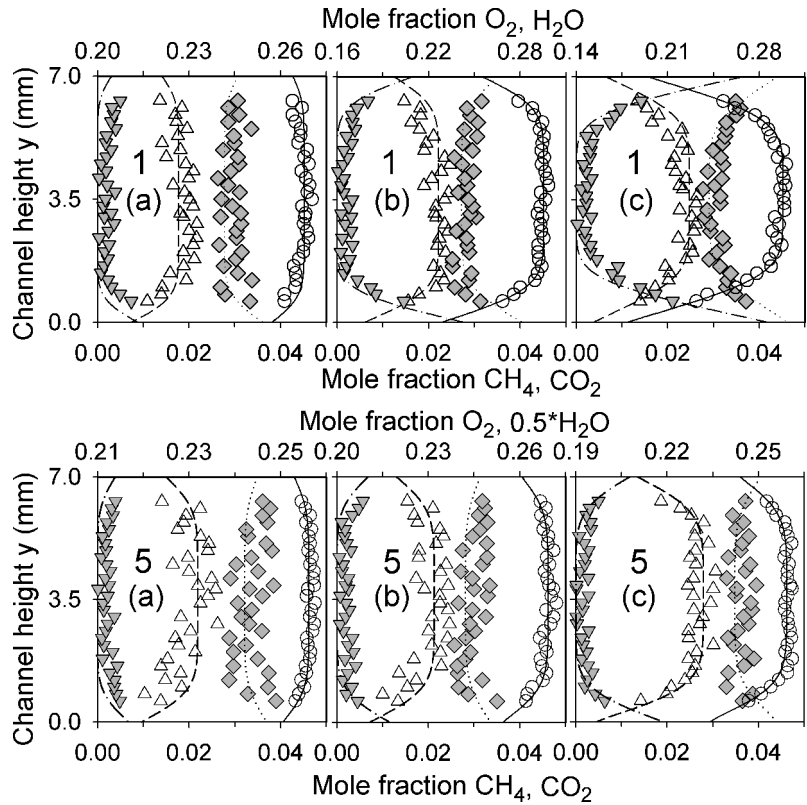

Figure 4. Comparisons between Raman-measured (symbols) and numerically predicted (lines) transverse profiles of species mole fractions at three selected axial positions of Cases 1 and 5 (Table 1). CH_4 (open circles, solid lines), O_2 (open upper triangles, dashed lines), H_2O (filled diamonds, dotted lines) and CO_2 (filled lower triangles, dashed-dotted lines). Case 1: (a) $x = 43$ mm, (b) $x = 73$ mm, (c) $x = 103$ mm. Case 5: (a) $x = 33$ mm, (b) $x = 43$ mm, (c) $x = 53$ mm. The narrower upper horizontal scale artificially increases the experimental scatter of O_2 and H_2O.
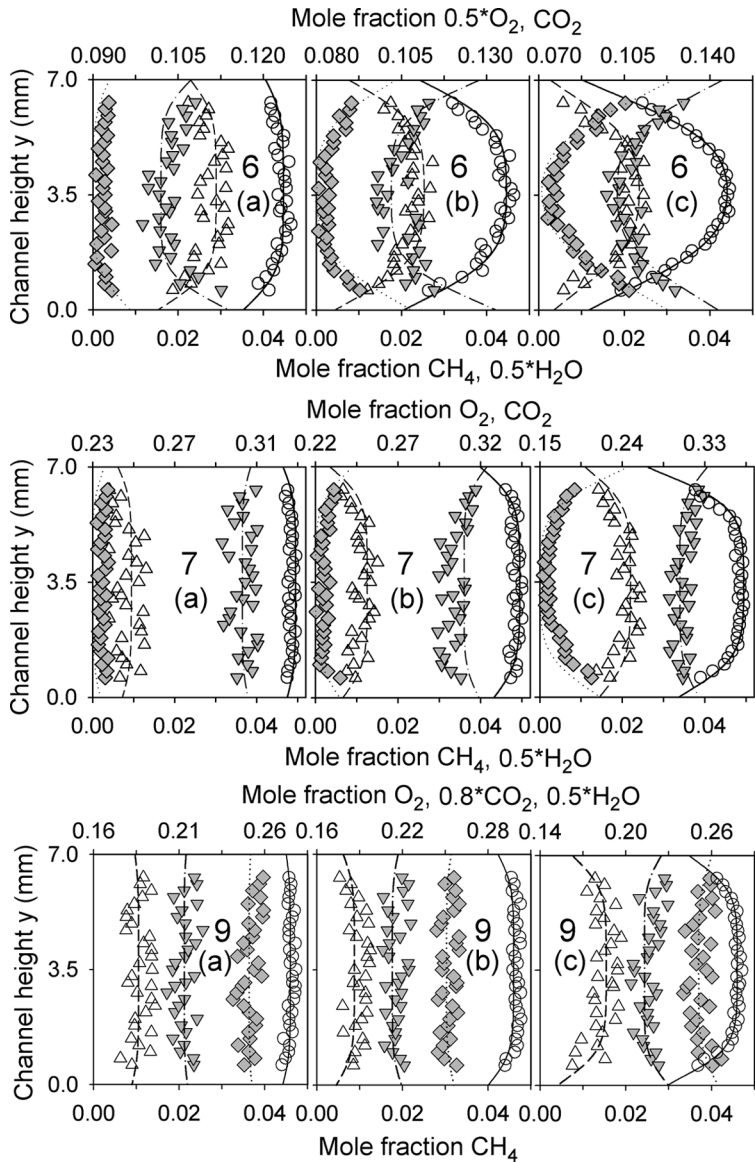
Figure 5. Comparisons between Raman-measured (symbols) and numerically predicted (lines) transverse profiles of species mole fractions of Cases 6, 7 and 9 (Table 1). The species notation is the same as in Fig. 4. Case 6: (a) $x = 43$ mm, (b) $x = 83$ mm, (c) $x = 123$ mm. Cases 7 and 9: (a) $x = 43$ mm, (b) $x = 63$ mm, (c) $x = 83$ mm. The narrower upper horizontal scale artificially increases the experimental scatter of the relevant species.

or predicted) exhibited a slight asymmetry due to temperature differences (up to 45 K, see Figure 3) between the upper and lower catalytic plates. The attainment of kinetically controlled catalytic conversion (manifested by the non-zero wall concentration of methane in Figures 4 and 5) required a careful control of the heating/cooling reactor mechanisms (discussed in the experimental section) in order to achieve suitable surface temperatures. Key to the determination of the catalytic reactivity was the near-wall bending in the boundary layer profile of methane, which was the deficient reactant. The near-wall profiles of Figures 4 and 5 were controlled by the balance between transverse fluid mechanical transport and catalytic reaction according to the interfacial boundary conditions of Eqs. (9).

Considering that laminar transport can be accurately modeled, the agreement between measurements and predictions reflected the aptness of the catalytic reaction scheme. The measurement accuracy was determined by recording the signals of pure CH_4, air and completely burned gases of known composition, as also stated in the preceding section on "Laser diagnostics." The CH_4 levels ranged from 2% to 5% per volume over the exploitable transverse extent of the Raman experiments ($0.6 \, mm \leq y \leq 6.4 \, mm$), resulting in a measurement accuracy of $\pm 5\%$ (i.e., up to 0.25% per volume). Over the same transverse extent, the levels of combustion-generated CO_2 (in cases with only H_2O dilution, see Figure 4) and H_2O (in cases with only CO_2 dilution, see Figure 5) ranged from nearly zero at the channel center ($y = 3.5 \, mm$) up to 4% vol. at the extreme measuring locations $y = 0.6$ and $6.4 \, mm$.

The experimental accuracy was $\pm 10\%$ for the near-wall zones with H_2O and CO_2 volumetric compositions greater than 0.5%, whereas the accuracy at the channel core with corresponding compositions less than 0.5% was poor. Nonetheless, the knowledge of the H_2O and CO_2 levels around the channel center was not required for the assessment of the catalytic reactivity. In addition, the near-wall H_2O and CO_2 measurements complemented-but did not control decisively-the kinetic validation since the formation of those species was directly linked to the consumption of CH_4 in the present complete oxidation studies. This was not, however, the case during partial oxidation (Appel et al., 2005a), where the presence of co-existing or sequential pathways (total and partial oxidation) required determination of all reactants and products.

The measured near-wall drop of CH_4 and rise of H_2O/CO_2 were captured well by the numerical predictions. It is worth noting that the

near-wall profiles of Figures 4 and 5, which were established by the trans-
verse transport-reaction balances of Eqs. (9), can qualitatively reveal cer-
tain parametric dependencies of the catalytic reactivity. For example, the
transverse wall gradients of methane at the upper wall ($y = 7$ mm) were
roughly the same in Figure 5(6a, 7a) that pertained to $x = 43$ mm. Since
Case 7 had an enhanced transverse fluid mechanical transport (it scaled
with Re_{IN} (Mantzaras and Benz, 1999)) and at the same time the upper-
wall temperature of Case 7 was lower by 20 K compared to that of Case 6
(see the temperature profiles of Figure 3(b, c) at $x = 43$ mm), Eqs. (9)
necessitated an increase in the catalytic reactivity for the higher pressure
Case 7 (the difference in CO_2 content is not relevant, because this dilu-
ent is chemically inert as will be shown in the next section; moreover, the
small difference in CH_4 content is overtaken by the Arrhenius exponen-
tial as can be shown by using the global step of the forthcoming Eq. (19)).
The above pressure enhancement of the catalytic reactivity has been
already established for CH_4/air catalytic combustion without dilution
(Reinke et al., 2004).

In summary, the overall good agreement between Raman measure-
ments and predictions for the pressures, surface temperatures, type
and amount of diluent in Figures 4 and 5 clearly demonstrated that
the employed catalytic scheme (Deutschmann et al., 2000) was appropri-
ate for fuel-lean catalytic combustion of methane with large exhaust gas
recycle. It will be, therefore, used in the ensuing simulations to investi-
gate the impact of dilution on the catalytic reactivity.

Impact of Water on the Catalytic Reactivity

To examine the effect of H_2O dilution, initially a sensitivity analysis (SA)
was carried out. The SA of Figure 6 has been constructed by multiplying
or dividing the pre-exponential A of every single reaction of Table 2 by a
given factor K and then computing the catalytic methane conversion at
the channel exit anew (gas-phase chemistry was not included). Factors
K equal to 10, 5 and 2 were used and all reproduced the same set of sig-
nificant reactions. The six most sensitive reactions are provided in Figure
6 for Cases 2 and 5 ($p = 5$ and 14 bar, respectively, with $\sim 50\%$ vol. H_2O
dilution). The CH_4 and O_2 adsorption (the former being the rate limiting
step) and the O_2 desorption (S1/S3, S19), were the most sensitive
reactions as they determined the rate of reactant depletion. Next in
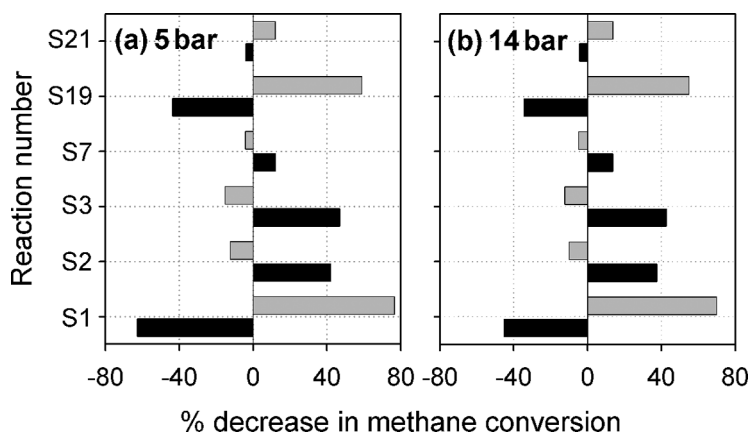significance were the H_2O adsorption (S7) and desorption (S21): a

Figure 6. Sensitivity analysis of the heterogeneous pathway for (a) Case 2, and (b) Case 5 of Table 1. The six most sensitive reactions (the reaction numbering follows Table 2) are provided. The reaction pre-exponentials have been increased (black bars) or decreased (gray bars) by a factor of 10.

multiplication (division) of the water adsorption rate reduced (increased) the methane catalytic conversion. Supplementary analyses have further shown that the sensitivity of the water adsorption/desorption reactions increased with growing water dilution.

Having established the importance of the water adsorption/ desorption reactions, a detailed analysis has followed to elucidate the chemical impact of H$_2$O on the heterogeneous pathway. SPSR computations have been carried out at fixed reactor pressures and temperatures and a surface-to-volume ratio $S/V = 2.86$ cm^{-1} (equal to that of the channel-reactor). Equations (11) were solved, without inclusion of gaseous chemistry ($\dot{\omega}_k = 0$). The computed catalytic methane conversions are provided in Fig. 7 as a function of reactor temperature for $\varphi = 0.40$ and a total dilution of 75.8% vol. consisting of water (30%, 50% and 75.8%) and nitrogen. The plots of Fig. 7 have been constructed as follows. A fictitious diluent species H$_2$O* was introduced that had the same thermodynamic properties as H$_2$O but did not participate in any catalytic reaction. H$_2$O* simulated only the dilution water whereas the catalytic pathway was still allowed to create combustion-generated H$_2$O. The residence times required to achieve a 5% methane conversion of the CH$_4$/O$_2$/H$_2$O*/N$_2$ mixtures (30%, 50% and 75.8% H$_2$O*) were initially computed using the SPSR model. Subsequently, the methane
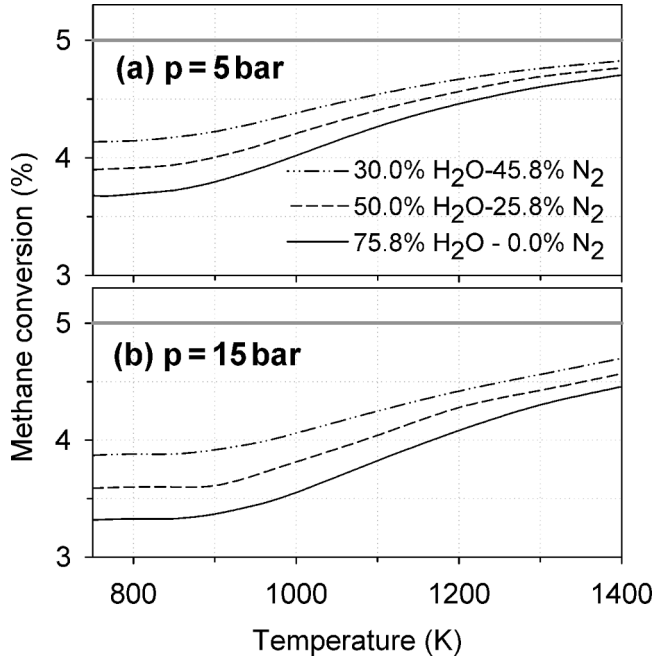
Figure 7. Computed methane conversions in a surface perfectly stirred reactor (SPSR) for $\phi = 0.4$, three different water dilutions and two pressures. The reactor residence times were those that produced a fixed 5% conversion when the corresponding H_2O dilution was replaced by inert H_2O^*.

conversions for the $CH_4/O_2/H_2O/N_2$ mixtures were calculated using the residence times of the corresponding H_2O^* dilutions. The plots of Fig. 7 clearly indicated that water dilution inhibited the catalytic reactivity. Using Eqs. (11), the balance of methane can be written as:

$$\frac{(Y_{CH4,IN} - Y_{CH4})}{\tau} = (1/\rho)(S/V)\dot{s}_{ads,CH4}W_{CH4} \tag{15}$$

with

$$\dot{s}_{ads,CH4} = k_{ads,CH4}[CH_4](\Gamma\theta_{Pt})^{2.3} \tag{16}$$

$\Gamma\theta_{Pt} = [Pt(s)]$ denotes the surface concentration of free sites and $[CH_4]$ the volumetric gas-phase methane concentration. In the provided catalytic scheme (Deutschmann et al., 2000), the adsorption of methane had a 2.3-order dependence on the free-site surface concentration

(see note in Table 2). The influence of the catalytic pathway was manifested in Eqs. (16) and (15) through the coverage term $\theta_{Pt}^{2.3}$. Provided that [CH₄] was the same, the changes in methane conversion reflected only free-site coverage differences. Hence, a small ($\leq 5\%$) methane conversion was imposed in the plots of Figure 7 in order to maintain a nearly constant [CH₄] for all cases. The decrease in heterogeneous conversion seen in Figure 7 was directly linked to the reduction of free platinum sites. The origin of the H₂O-related decrease in θ_{Pt} has been further elaborated with the reaction flux analysis of Figure 8 and the surface coverage of Figure 9.

Figure 8 provides SPSR-computed heterogeneous fluxes (no gas-phase chemistry included) at $p = 15$ bar, $T = 1000$ K, $\tau = 32$ ms with 75.8% vol. H₂O or H₂O* dilution. The initiating reactions were the dissociative adsorption of CH₄ and O₂, the main surface steps were the oxidation of H(s) and C(s) to OH(s)/H₂O(s) and CO(s)/CO₂(s) and, finally, the desorption of H₂O(s) and CO₂(s) provided the main gas-phase products. The comparisons in Figure 8(a, b) revealed that the H₂O dilution increased by a factor of 160 the water adsorption and desorption rates (S7, S21). Similarly, the H₂O dilution yielded higher H₂/OH adsorption (S4, S8) and desorption rates (S20, S22) by a factor of 117 and 12, respectively, and a lower CH₄ adsorption rate (S1) by a factor of 0.7. A first supposition that the reduction in Pt(s) sites could have been caused by a higher H₂O surface coverage due to the increased water partial pressure was not supported by the following analysis.

The surface coverage is given in Figure 9 for the 75.8% H₂O (solid lines) and 75.8% vol. H₂O* (dotted lines) dilution as a function of SPSR temperature; it is seen that the H₂O dilution caused an increase in θ_{H2O}, θ_{OH} and θ_{H} at the expense of θ_O, θ_{Pt}, and to a lower degree, of the C-containing surface species. The increase in θ_{H2O} ranged from ca·10^{-6} 6 to 10^{-4}; however, those magnitudes were too low to appreciably affect the dominant Pt(s) and O(s) coverage. For temperatures between 750 and 1400 K and residence times as low as 2 ms (ranges of interest to practical combustors), the surface reactions S10–S12 were in partial equilibrium. Hence, the equilibrium constants of the dominant water-producing reaction S12 and of the OH(s)-forming step S10 (see Table 2) were:

$$K_{c,S12}(T) \approx \frac{[H_2O(s)] \cdot [O(s)]}{[OH(s)]^2} = \frac{\theta_{H2O}\theta_O}{\theta_{OH}^2} \qquad (17)$$
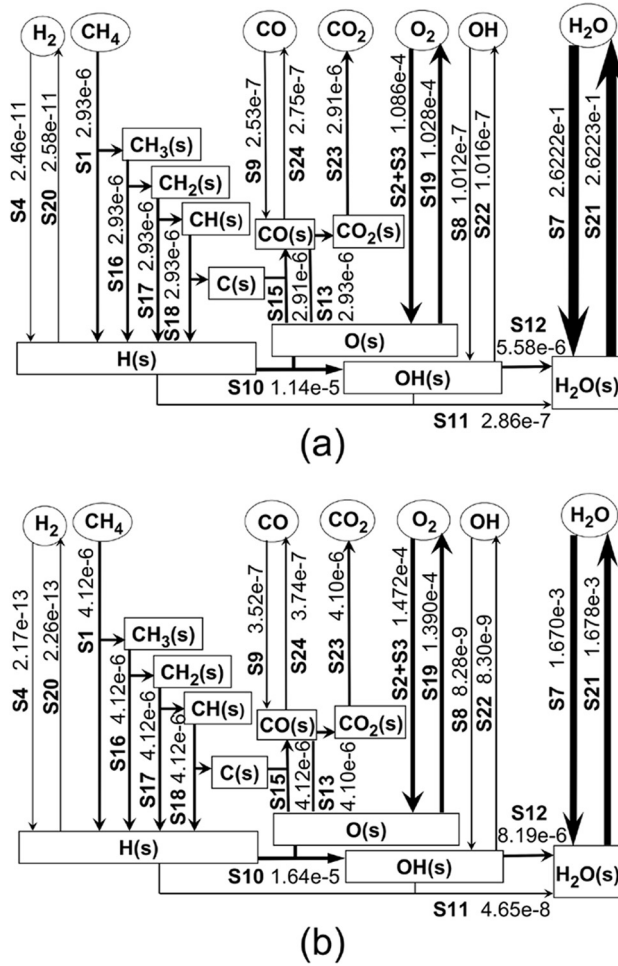
Figure 8. Reaction flux (mol/cm^{2}sec) calculated in a surface perfectly stirred reactor (SPSR) at $\varphi = 0.4$, $p = 15\,\text{bar}$, $T = 1000\,\text{K}$, $S/V = 2.86\,\text{cm}^{-1}$ and $\tau = 32\,\text{ms}$: (a) 75.8% H_2O dilution and (b) 75.8% H_2O^* inert dilution. The reaction numbering follows Table 2.

$$K_{c,S10}(T) \approx \frac{[\text{OH(s)}] \cdot [\text{Pt(s)}]}{[\text{H(s)}] \cdot [\text{O(s)}]} = \frac{\theta_{\text{OH}}\theta_{\text{Pt}}}{\theta_{\text{H}}\theta_{\text{O}}} \tag{18}$$

According to Eq. (17) an increase in θ_{H2O} at a given reactor temperature led to an increase in θ_{OH}, which was appreciable in absolute numbers (e.g., from 3.5×10^{-3} to 0.045 at $T = 1000\,\text{K}$, see Figure 9) and could thus
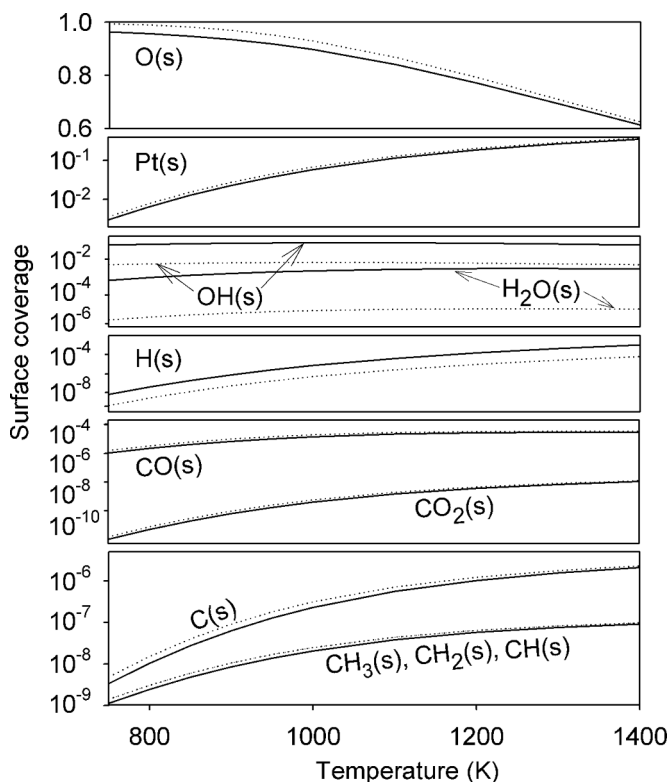
Figure 9. Surface coverage computed in a surface perfectly stirred reactor (SPSR) at different reactor temperatures. Solid lines: 75.8% H_2O dilution, dotted lines: 75.8% H_2O^* inert dilution. The other reactor parameters are as in Figure 8.

impact the coverage of the major surface species Pt(s) and O(s). The increase in θ_{OH} caused also a rise in θ_H due to Eq. (18) which, nonetheless, did not affect θ_O and θ_{Pt}. Overall, the water dilution inhibited the catalytic activity due to the increased surface coverage of OH(s). The increase in θ_{OH} also augmented the OH desorption fluxes ($=k_{des,OH}\Gamma\theta_{OH}$), which could potentially affect gas-phase ignition. This issue will be elaborated in the homogeneous combustion section.

The influence of H_2O amount, pressure, and temperature on the catalytic reactivity is elaborated next. Increasing the H_2O dilution further inhibited the catalytic reactivity (Figure 7). Increasing the pressure at constant H_2O dilution and temperature accentuated the catalytic

inhibition (Figure 7). This was an outcome of the higher partial pressure of H_2O causing an increase of the H_2O adsorption and desorption rates that resulted in a drop of the Pt(s) coverage (i.e., of the vacant sites). Finally, a reduction of the surface temperature decreased the catalytic reactivity and this effect was more pronounced at larger H_2O dilutions (Figure 7) due to the strong temperature dependence of the controlling reaction S12 (The equilibrium constant $K_{c,S12}$ calculated with the thermodynamic data of Warnatz et al. (1994) decreased with declining temperature). For a given θ_{H2O}, a drop in temperature led to increased θ_{OH} according to Eq. (17) and the temperature dependence of $K_{c,S12}$. At the same time, θ_{Pt} was also reduced drastically due to the much more efficient oxygen adsorption at lower temperatures (Deutschmann et al., 1996). Therefore, the relative decrease in θ_{Pt} due to the increase in θ_{OH} was more pronounced at lower temperatures, leading to a stronger inhibition of the catalytic reactivity.

Extensive SPSR computations at different pressures, temperatures and water dilutions were carried out to quantify the water inhibition. The following global step reproduced with a relative error of less than $\pm 25\%$ the computed methane conversions of the detailed catalytic scheme (Deutschmann et al., 2000):

$$\dot{s}_{CH4} = B \exp(-E_a/RT)[CH_4][H_2O]^{-0.36} \tag{19}$$

with $B = A(p/p_o)^{-0.53}$, $A = 2.3 \times 10^7 \, \text{mol}^{0.36} \, \text{cm}^{-0.08} \text{sec}^{-1}$, $p_o = 1 \, \text{bar}$, and effective activation energy $E_a = 163 \, \text{kJ/mol}$. The negative pressure dependence $p^{-0.53}$ in the pre-exponential factor B was not related to water dilution and it accounted for the reduction in free platinum sites with increasing pressure (Reinke et al., 2004; Snow et al., 1984). Given the fact that $[CH_4] \propto p$, the $p^{-0.53}$ dependence restrained the rate of increase of the catalytic reactivity with increasing pressure in standard CH_4/air combustion. The exponent -0.36 in the water concentration was comparable to that proposed for Pd at $T < 823 \, \text{K}$ and $p = 1 \, \text{bar}$ (Ibashi et al., 2003). The relation of Eq. (19) was valid for $5 \, \text{bar} \leq p \leq 15 \, \text{bar}$, $800 \, \text{K} \leq T \leq 1250 \, \text{K}$, equivalence ratios of 0.5 and 0.4, water dilutions from 25% to 75% per vol., and a wide range of residence times that yield methane conversions from 5% to 99% (see Figure 10).

In summary, the water dilution led to an inhibition of the catalytic reactivity that was more pronounced at lower surface temperatures,
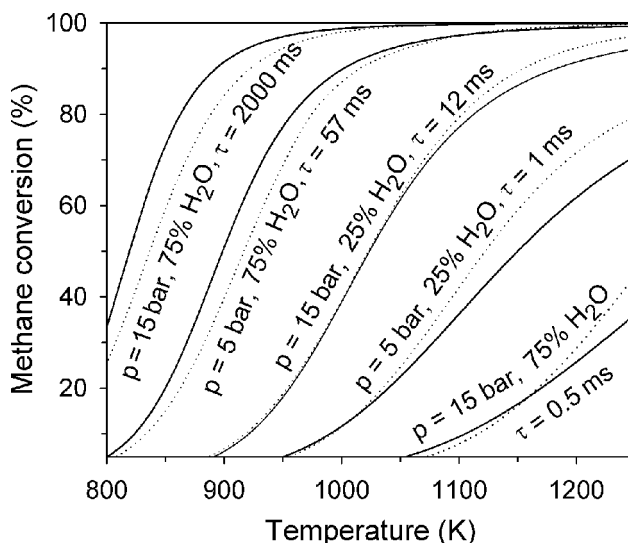
Figure 10. Computed methane conversion in a surface perfectly stirred reactor (SPSR) for a $\varphi = 0.40$ CH$_4$/O$_2$ mixture with a 75% vol. combined H$_2$O and N$_2$ dilution. The surface-to-volume ratio is 100 cm^{-1}. Calculations for 5 and 15 bar and water dilutions of 25% and 75% are presented; for each condition the residence times are varied so as to achieve different conversions. Solid lines: full heterogeneous scheme of Table 2; dotted lines: one-step catalytic reaction of Eq. (19).

higher pressures, and larger H$_2$O dilutions. For practical combustion approaches (Griffin et al., 2004), the associated large water dilution ($\geq 60\%$) has to be considered in the reactor design. It is fortunate that in the aforementioned approaches the inlet temperatures can reach up to 1150 K, thus moderating the negative impact of water dilution on the catalytic reactivity. It is also noted that in steady, fuel-lean CH$_4$/air (no H$_2$O dilution) catalytic combustion, the inhibition due to water formation is not a controlling factor: for a diffusionally neutral fuel such as methane (Lewis number ~ 1) the combustion-generated H$_2$O near the wall does not exceed the value dictated by the reaction stoichiometry (e.g., only up to 10% vol. H$_2$O for $\varphi = 0.50$). In fuel-lean H$_2$/air combustion, however, the water inhibition can become significant as the low Lewis number of hydrogen causes an effective catalytic stoichiometry twice that of the gaseous phase (Appel et al., 2002; Bui et al., 1996).

Impact of CO_2 on the Catalytic Reactivity

The employed scheme (Deutschmann et al., 2000) did not include a CO_2 adsorption step (see Table 2), and hence the gas-phase CO_2 could not couple chemically to the catalytic pathway. The good agreement between measurements and predictions in Figure 5 supported this conclusion. Nonetheless, the effect of CO_2 was further elaborated by augmenting the original catalytic scheme with additional CO_2-related surface reactions from other literature mechanisms. A non-activated CO_2 adsorption with sticking coefficient of unity as well as the additional surface reactions $CO(s) + OH(s) = CO_2(s) + H(s)$ and $2CO(s) = C(s) + CO_2(s)$ (Aghalayam et al., 2003) were introduced in the original scheme of Deutschmann. The inclusion of those reactions together with the additional surface species $CO_2(s)$ led to negligible changes in the SPSR-predicted surface coverage and methane conversions. The same was also attested when–in addition to the previous changes–the kinetic parameters of $CO_2(s)$ desorption (S23) were exchanged to those of Aghalayam et al. (2003). The previous procedure was also repeated by including four new reactions from the work of Zerkle et al. (2000), which were $CO_2 + Pt(s) \rightarrow CO_2(s)$, $CO_2(s) + Pt(s) \rightarrow CO(s) + O(s)$, $CO(s) + OH(s) \rightarrow CO_2(s) + H(s)$ and $CO_2(s) + H(s) \rightarrow CO(s) + OH(s)$, and further exchanging the kinetic parameters of S23 with those of Zerkle et al. SPSR computations over the temperature range $600\,K \leq T \leq 1600\,K$ with CO_2 dilutions up to 30% vol. indicated that the addition of this reaction subset and of the species $CO_2(s)$ had a negligible influence on the catalytic reactivity.

The impact of CO_2 on the catalytic pathway through a hetero/homogeneous chemistry coupling was also investigated. A fictitious species CO_2^* was introduced, which had the same thermodynamic properties and third body efficiency in all gas-phase reactions as CO_2. SPSR predictions with the Deutschmann/Warnatz hetero-/homogeneous schemes for $CH_4/O_2/N_2/CO_2$ and $CH_4/O_2/N_2/CO_2^*$ mixtures revealed that at high temperatures the dissociation of CO_2 caused a rise in CO and thus of CO(s) coverage that, in turn, increased the catalytic methane conversion. Nonetheless, this increase was less than 1% over the temperature range $600\,K \leq T \leq 1600\,K$. It is finally clarified that the analyses in the last two sections have isolated the chemical impact of H_2O and CO_2 dilution since the SPSR or the channel-reactor surface temperatures were prescribed. In practical CST systems, thermal effects (due to the

larger heat capacity of those species compared to N_2) should also be accounted for.

HOMOGENEOUS COMBUSTION

Comparisons of Measurements and Predictions

Gas-phase combustion has been investigated in Cases 10–14, whereby the higher surface temperatures allowed for homogeneous ignition and flame formation. For a proper investigation of the gaseous pathway, an assessment of the catalytic processes preceding the onset of homogeneous ignition was still necessary. Even though the scheme of Deutschmann et al. (2000) has been validated in the foregoing section, the relatively high surface temperatures required to achieve homogeneous ignition could potentially deactivate (partially or totally) the catalyst, thus creating a near-wall fuel excess. This fuel excess could, in turn, promote the onset of homogeneous ignition (Mantzaras and Appel, 2002) and hence falsify the assessment of the gaseous reactivity. Comparisons between Raman-measured and predicted (Deutschmann/ Warnatz reaction schemes) transverse profiles of species mole fractions are provided in Figure 11 for Cases 11 and 12. All axial positions of Case 11 and the first two of Case 12 were located upstream the onset of homogeneous ignition (x_{ig}), measured or predicted, as seen by the OH maps of Figure 12. Moreover, at the first axial position (Figure 11(11a, 12a)) the gas-phase contribution was minimal as will be discussed in the forthcoming Figure 17. The very good agreement between measurements and predictions in Figure 11 suggested that the catalytic scheme realistically reproduced the heterogeneous processes over the entire gaseous induction zone.

Typical measured surface temperature profiles are provided in Figure 13 for three selected cases; the temperatures spanned the range 1120 to 1380 K and were 200 to 300 K higher compared to those of the catalytic combustion studies (Figure 3). Over the induction zone $0 \leq x \leq x_{ig}$ the upper and lower wall temperatures differed by as much as 32 K, leading only to slight asymmetries in the Raman profiles of Figure 11. This was attributed to the nearly mass-transport-limited catalytic conversion of methane (manifested by the low CH_4 levels near both walls in Figure 11(11a, 12a)), which rendered the catalytic processes relatively insensitive to small surface temperature variations. The
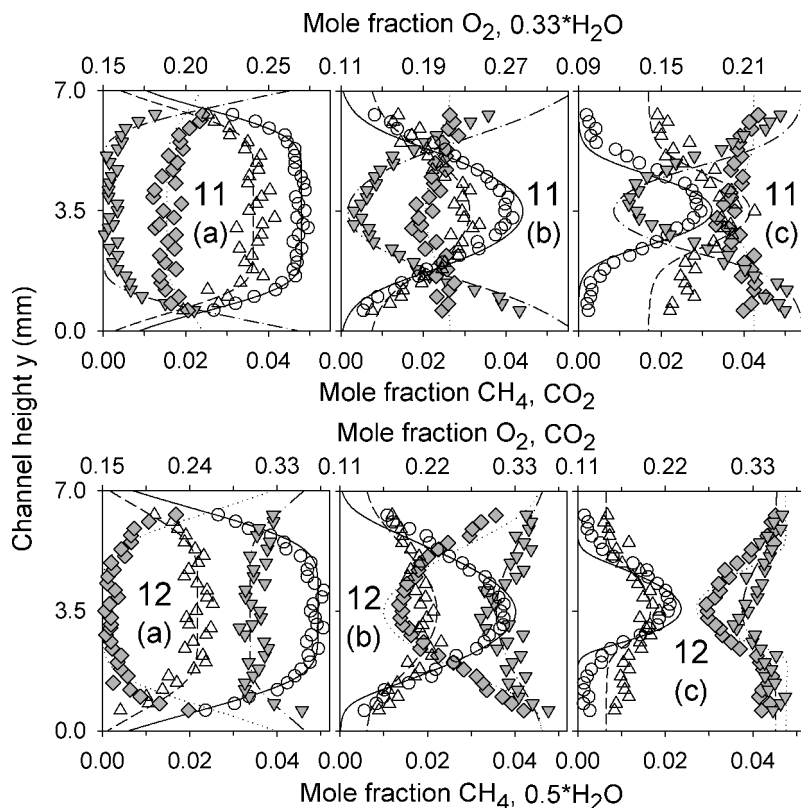
Mole fraction O_2, 0.33*H_2O

Figure 11. Comparisons between Raman measured (symbols) and numerically predicted (lines) transverse profiles of species mole fractions for Cases 11 and 12 of Table 1. The species notation is the same as in Figure 4; (a) $x = 12$ mm, (b) $x = 93$ mm, (c) $x = 153$ mm.

contribution of the gaseous pathway was non-negligible in Figure 11(11b, 11c, 12b) even though those positions were upstream of x_{ig}. The profiles in Figure 11(12c) were located downstream the homogeneous ignition location and were greatly impacted by the gaseous pathway, as manifested by the lack of CH_4 in extended zones near both walls. Those issues will be elaborated in the last section.

Comparisons between LIF-measured and computed (Deutschmann/Warnatz schemes) distributions of the OH radical are illustrated in Figure 12. The stability and reproducibility of the measured flames was excellent. Pressures $p \geq 12$ bar were used in the H_2O dilution cases. Since the safe operation of the steam generator required a minimum
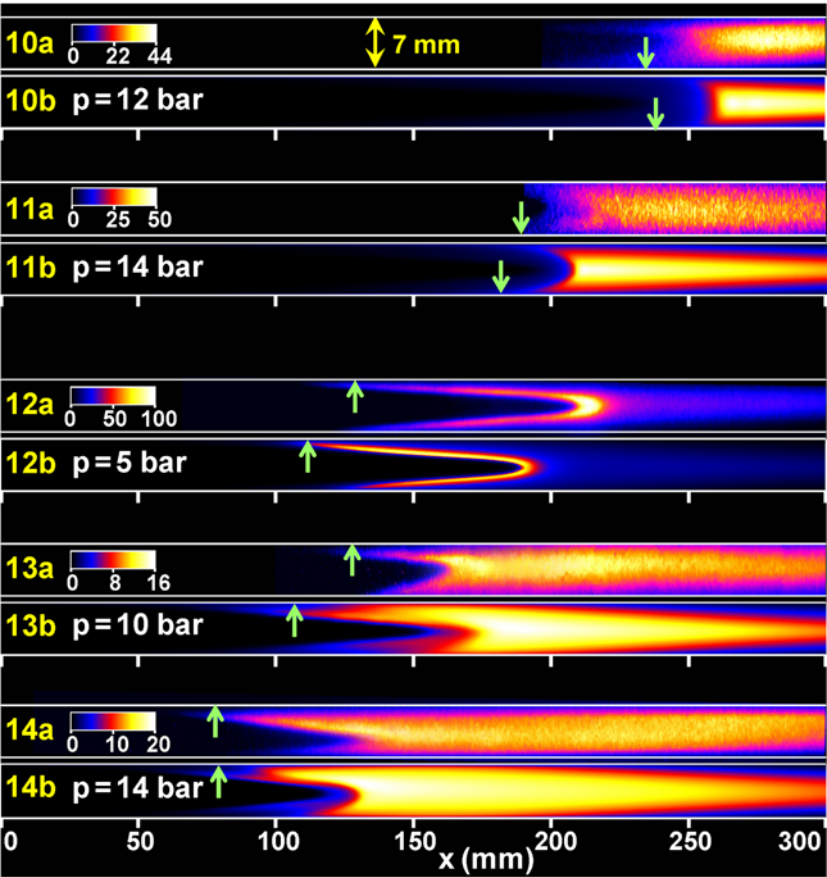
Figure 12. (a) LIF-measured, and (b) numerically predicted distributions of the OH radical for Cases 10 to 14 of Table 1. The green arrows define the onset of homogeneous ignition. The color bars provide the OH levels (ppmv).

amount of H_2O production, inlet Reynolds numbers no less than ~ 1500 had to be used: under those conditions there were sufficient residence times for gas-phase ignition only for the more reactive higher-pressure cases. The flames of Figure 12 exhibited a slight-to-moderate asymmetry depending on the temperature differences between the two catalytic walls. Given the particular sensitivity of homogeneous ignition on the wall temperature (Mantzaras and Appel, 2002; Mantzaras and Benz, 1999), the asymmetries in the flames of Figure 12 were more
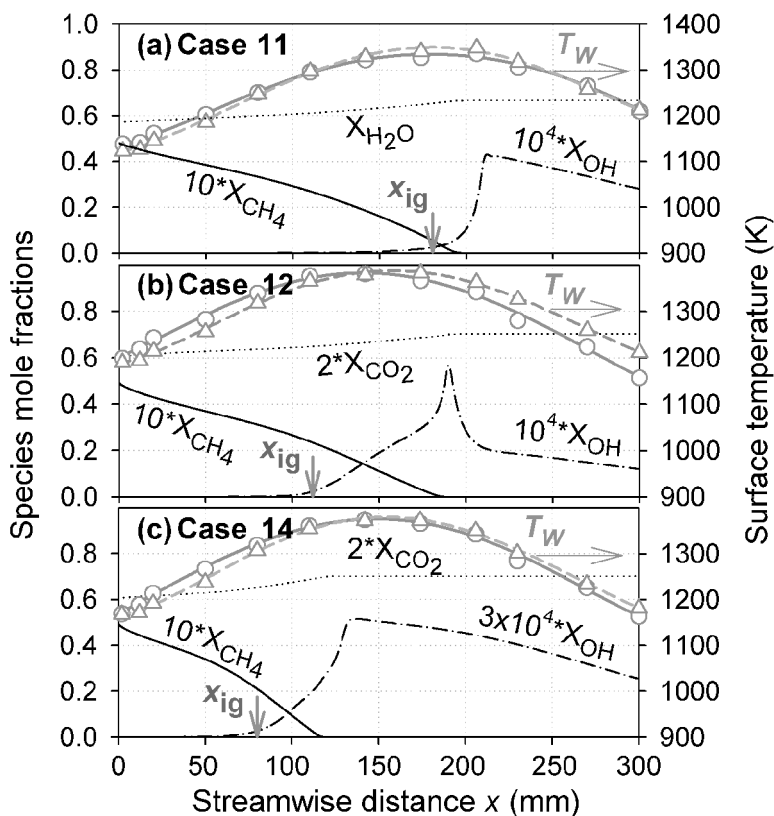
Figure 13. Computed streamwise profiles of transversely-averaged species mole fractions for three cases of Table 1: CH_4 (solid lines), H_2O or CO_2 (dotted lines) and OH (dashed-dotted lines). The onset of homogeneous ignition is identified by the arrows marked x_{ig}. The symbols give the measured surface temperatures and the gray lines are fits through them: upper plate (circles, gray solid lines), lower plate (triangles, gray dashed lines).

pronounced compared to those of the species transverse profiles of Figure 11. The predicted homogeneous ignition position (indicated with the green arrows in Figure 12) was determined from Figure 13, which provided the averaged (over the 7-mm transverse distance) axial profiles of CH_4, H_2O/CO_2 and OH mole fractions; the axial position with OH intensity amounting to 5% of the peak intensity was used to define homogeneous ignition (x_{ig}). A similar procedure was used to determine the measured x_{ig}. The lower-pressure flame of Case 12 had the highest

OH mole fractions with peak values relaxing rapidly in the post-flame zone (see Figure 12(12a,b)). The higher-pressure flames had lower OH mole fractions that were, however, maintained over a longer post-flame extent. The lower superequilibrium OH flame mole fractions were caused by the increased importance of three-body radical recombination reactions at high pressures.

The LIF-measured onset of homogenous ignition was captured well by the Deutschmann/Warnatz schemes in the water dilution cases; for example, in Cases 10 and 11 the differences between measured and predicted x_{ig} were less than 3.5% (Figure 12). The measurements and predictions with CO$_2$ dilution were also in good agreement with each other (x_{ig} within 14%). In addition, the measured flame shapes and OH levels of Figure 12 were well reproduced by the predictions. Overall, the gas-phase scheme of Warnatz et al. (1996)—when used in conjunction with the catalytic scheme of Deutschmann et al. (2000)—was suitable for hetero-/homogeneous combustion of CH$_4$ with large exhaust gas dilution.

Impact of H$_2$O and CO$_2$ on Homogeneous Ignition

The impact of H$_2$O dilution was investigated first with ignition delay studies of pure gaseous mixtures. This was to avoid inherent interferences from the preceding catalytic pathway, which was also significantly affected by water addition. Normalized ignition delay times computed in a batch reactor of fixed pressure and temperature are provided in Figure 14. The fixed temperature mimicked the presence of the catalytic pathway that supplied heat to the gas. Equations (13) were solved and the ignition delays were defined as the times corresponding to 50% methane conversion. For the construction of Figure 14, the ignition delay times of a $\varphi = 0.40$ CH$_4$/O$_2$/H$_2$O* mixture with 75.8% vol. H$_2$O* dilution were initially calculated (H$_2$O* had the same thermodynamic properties and third body efficiency with H$_2$O but did not participate explicitly in any gas-phase reaction). Subsequently, part of H$_2$O* was exchanged by H$_2$O and the resulting ignition delay times were normalized by the corresponding times of 75.8% H$_2$O* dilution. For a given pressure and temperature, the ignition delay times decreased with increasing H$_2$O dilution (Figure 14), clearly showing that water promoted chemically homogeneous ignition. In addition, the chemical promotion was more pronounced at higher pressures and lower temperatures.
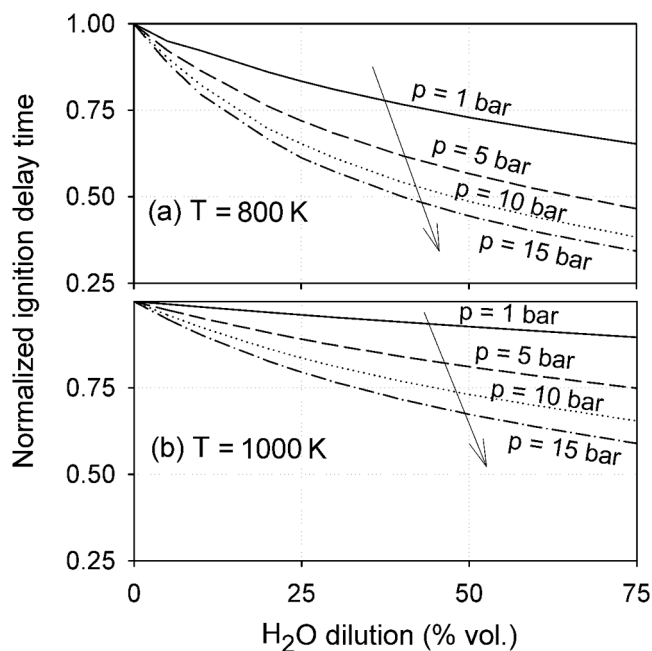
Figure 14. Normalized ignition delay times for a CH_4/O_2 mixture ($\phi = 0.40$) with 75.8% vol. dilution comprising of H_2O and chemically inert H_2O^*. The normalization is done with the corresponding delay of the 75.8% vol. H_2O^* mixture. The computations refer to fixed pressures and temperatures: (a) 800 K and (b) 1000 K.

The impact of H_2O dilution was subsequently investigated in the channel reactor. Replacing H_2O with H_2O^* resulted in a significant increase of x_{ig} (in Case 11, for example, x_{ig} increased by 50 mm) indicating that water promoted homogeneous ignition. It is noted that only a small part of the increase in x_{ig} was attributed to the enhancement of the catalytic activity (and hence to the increase in heterogeneous methane conversion at the expense of the homogeneous pathway) when H_2O was replaced by H_2O^*. This was because the heterogeneous conversion was already close to the mass-transport-limit; this effect alone contributed only to a 6 mm increase in x_{ig}. Therefore, the hetero-/homogeneous simulations have also indicated that water promoted chemically the reactivity of the gaseous pathway. The origin of the chemical promotion will be elaborated in the following section. Although the chemical impact was of main interest in this study, thermal effects were also assessed

by exchanging the volumetric amount of H$_2$O by N$_2$ and re-computing x_{ig}. When H$_2$O was replaced by N$_2$, the onset of homogeneous ignition in Figure 13a shifted 70 mm upstream due to the nearly 30% larger heat capacity of the former species over the temperature range 800 to 1200 K (e.g., $c_{pH_2O} = 43.7\,\text{J/mol} \cdot \text{K}$ and $c_{p,N2} = 33.6\,\text{J/mol} \cdot \text{K}$ at 1200 K). Overall, when operating with large water dilutions, the thermal inhibition overtakes the chemical promotion of homogeneous ignition.

Ignition delay analyses with a fictitious species CO$_2^*$ revealed a negligible chemical impact of CO$_2$ addition (up to 30% vol.) on homogenous ignition. Furthermore, the channel computations yielded only a small reduction of x_{ig} when CO$_2$ was replaced by CO$_2^*$ (e.g., by 4 mm in Figure 13b). However, CO$_2$ inhibited thermally to a large degree homogeneous ignition due to its large heat capacity: for example, exchanging the volumetric CO$_2$ content by N$_2$ reduced the x_{ig} in Figure 13b by 80 mm.

Coupling of H$_2$O and CO$_2$ with Gaseous Chemistry and Hetero-/Homogeneous Interactions

The chemical impact of H$_2$O on the gas-phase pathway is elaborated next. A sensitivity analysis (SA) was carried out to identify the most important gas-phase chemical reactions affecting homogenous ignition. The pre-exponentials of all gaseous reactions were multiplied/divided by a factor of two and the x_{ig} were recomputed using the unaltered catalytic scheme of Deutschmann. The 12 most sensitive reactions affecting homogenous ignition are provided in Figure 15 (Case 11) for H$_2$O and H$_2$O* dilutions. In both SA of Figure 15 the chain terminating step HO$_2$ + OH=H$_2$O + O$_2$ (R3) and the methane depletion CH$_4$ + OH=H$_2$O + CH$_3$ (R11) were the most sensitive reactions. The axial profiles of O, H and OH mole fractions are plotted in Figure 16 for the H$_2$O and H$_2$O* dilutions of Case 11. Dilution with water increased appreciably the OH and mildly the H and reduced somewhat the O levels; those results were also attested qualitatively in the batch reactor ignition delay studies. The sensitivity of the reverse R12 (CH$_3$O$_2$H + OH=CH$_3$O$_2$ +H$_2$O) and R4 (H$_2$O$_2$ + OH=H$_2$O + HO$_2$) reactions (they both proceeded in the backward direction), increased with growing H$_2$O dilution; this led to higher OH concentrations that promoted the onset of homogeneous ignition. Over the induction zone, the rates of the (reverse) reactions R12 and R4 were one magnitude larger for H$_2$O compared to H$_2$O* dilution.
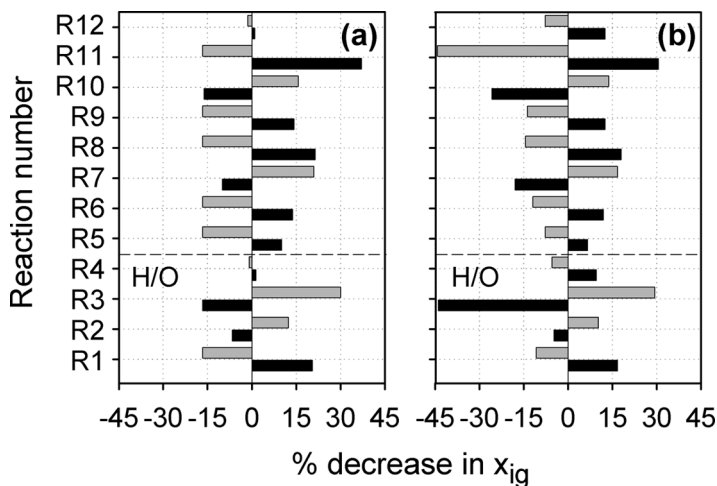
Figure 15. Sensitivity analysis of the gaseous pathway for Case 11 of Table 1 with (a) chemically inert H_2O^* dilution and (b) H_2O dilution. The 12 most sensitive reactions for the scheme of Warnatz (Warnatz et al., 1996) are provided. The reaction pre-exponentials have been increased (black bars) or decreased (gray bars) by a factor of two. R1: $O_2 + H = OH + O$, R2: $H + O_2 + M = HO_2 + M$, R3: $HO_2 + OH = H_2O + O_2$, R4: $H_2O_2 + OH = H_2O + HO_2$, R5: $CO + OH = CO_2 + H$, R6: $CO + HO_2 = CO_2 + OH$, R7: $CH_2O + OH = CHO + H_2O$, R8: $CH_2O + HO_2 = CHO + H_2O_2$, R9: $CH_3 + O_2 \rightarrow CH_2O + OH$, R10: $CH_3 + HO_2 = CH_4 + O_2$, R11: $CH_4 + OH = H_2O + CH_3$, R12: $OH + CH_3O_2H = H_2O + CH_3O_2$.

In a fashion similar to the water analysis, SA indicated that CO_2 did not impact appreciably the gas-phase reactions that controlled homogeneous ignition. Chemical effects of CO_2 dilution have been reported (Liu et al., 2003) for the propagation characteristics (laminar flame speeds) of methane mixtures and not for ignition delays that are relevant to the present homogeneous ignition studies. In the aforementioned work, it was found that for equivalence ratios $\varphi \geq 0.6$ (outside the range of CST) the addition of CO_2 reduced the burning velocities due to the reverse reaction $CO + OH = CO_2 + H$ that competed effectively with the chain branching reaction $H + O_2 = O + OH$ for H radicals.

Computed axial profiles of local catalytic and gaseous methane conversions are provided in Figure 17. Significant gas-phase methane conversion preceded the onset of homogeneous ignition (x_{ig}) and this was more pronounced at high pressures. The onset of appreciable gas-phase conversion was at $x_{ag} \approx 15$ mm in both cases of Fig. 17. To elucidate the
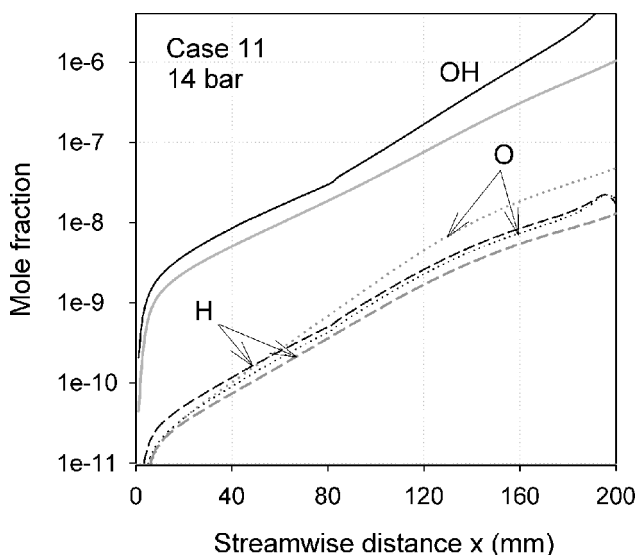
Figure 16. Computed axial profiles of OH, H and O radical mole fractions (averaged over the 7-mm transverse distance) for Case 11 of Table 1. Black lines: H_2O dilution; gray lines: chemically inert H_2O^* dilution. OH: solid lines; H: dashed lines; O: dotted lines.

hetero-/homogenous chemistry coupling, a carbon reaction flux analysis was carried out in an SPSR with 75.8% vol. H_2O dilution (Figure 18). Methane was oxidized in the gas-phase to CO, which adsorbed very efficiently on the Pt catalyst due to its very high sticking coefficient (S9 in Table 2). The adsorbed CO was oxidized catalytically to $CO_2(s)$ that further desorbed. Gas-phase hydrocarbon combustion can be generally described by a two-step process, the first being an incomplete reaction to CO and the second the main exothermic oxidation of CO to CO_2 (Westbrook and Dryer, 1981). The catalytic pathway inhibited homogeneous ignition by depriving CO from the gas-phase. Therefore, even in the absence of homogeneous ignition, the gaseous pathway could amount to significant methane conversion (particularly at higher pressures) through the incomplete oxidation of CH_4 to CO. The aforesaid hetero-/homogeneous coupling was general and not specific to H_2O and CO_2 dilution. However, the H_2O dilution accentuated the homogeneous contribution due to the increased reactivity of the gaseous pathway with increasing water content and the corresponding drop in the catalytic reactivity. The enhancement of the gaseous reactivity can be
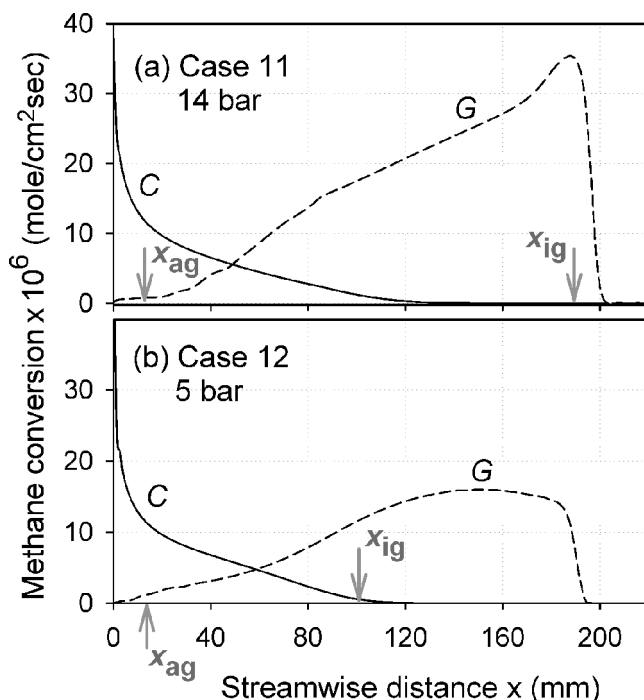
Figure 17. Computed streamwise profiles of catalytic (C, solid lines) and gaseous (G, dashed lines) methane conversions for two cases of Table 1. The onset of appreciable gaseous conversion and the onset of homogeneous ignition are identified by the arrows marked x_{ag} and x_{ig}, respectively.

seen as an advantage for combustion processes that utilize exhaust recycle (Griffin et al., 2004) since the ignition and stabilization of homogeneous combustion is particularly challenging in standard CST of natural gas/air mixtures.

The good agreement between measurements and numerical predictions at $x_{ag} \le x \le x_{ig}$ (Figure 11(11b, 11c, 12b)) has further suggested that the gas-phase scheme realistically reproduced the pre-ignition gas-phase chemistry. The comparisons of OH (Figure 12) and of the major species at post-ignition locations (Figure 11(12c)) also attested that the propagation characteristics were captured by the gaseous scheme.

The hetero-/homogeneous radical coupling is finally addressed. As discussed in the catalytic combustion section, the H_2O dilution increased the net desorptive fluxes of OH by an order of magnitude (see Figure 8).
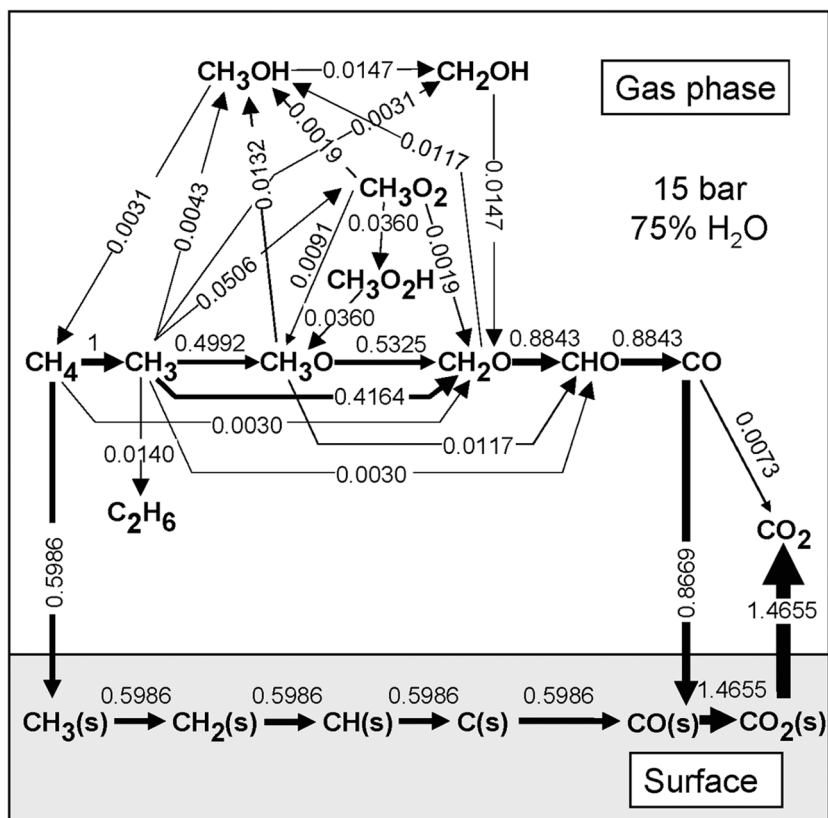
Figure 18. Heterogeneous and homogeneous reaction flux analysis in a surface perfectly stirred reactor (SPSR); CH$_4$/O$_2$ ($\varphi = 0.40$) with 75.% vol. H$_2$O dilution, $p = 15$ bar, surface to volume ratio $S/V = 2.86\,\text{cm}^{-1}$, reactor temperature $T = 1000\,\text{K}$ and residence time $\tau = 30\,\text{ms}$. The fluxes are normalized to the CH$_4\rightarrow$CH$_3$ flux. Only fluxes greater or equal to 0.0019 are shown.

The influence of the higher OH fluxes on the onset of homogenous ignition was investigated by modifying the adsorption and desorption steps (S8, S22) such that the catalytic pathway produced a fictitious gaseous species OH*, which did not participate in any gas phase reaction. Computations with the modified and the original catalytic scheme yielded practically the same x_{ig}. Even though the water dilution increased the OH catalytic fluxes by a factor of ten, their absolute magnitude was still too low to have an appreciable impact on the gaseous pathway. This outcome was similar to that reported for not-diluted CH$_4$/air mixtures

(Reinke et al., 2005) and indicated that the radical hetero-/homogeneous coupling was particularly weak even under high water dilutions.

CONCLUSIONS

The impact of large H_2O and CO_2 dilution (up to 59.5% H_2O and 30.3% CO_2 vol.) on the steady catalytic and gas-phase combustion of fuel-lean $CH_4/O_2/N_2$ mixtures over Pt was investigated experimentally and numerically at elevated pressures. To this task, in situ Raman and planar OH-LIF measurements have been used in conjunction with detailed numerical predictions. The following are the key conclusions of this study.

1. Comparisons between Raman-measured and predicted transverse profiles of major species concentrations have shown that the catalytic scheme of Deutschmann et al. (2000) captured the impact of H_2O or CO_2 addition on the catalytic reactivity over the pressure and surface temperature ranges 5 bar $\leq p \leq 14$ bar and 825 K $\leq T \leq 1180$ K, respectively. Comparisons between LIF-measured and predicted homogeneous ignition distances have also indicated that the gas-phase scheme of Warnatz et al. (1996) was suitable for fuel-lean combustion of CH_4/O_2 with large dilution of H_2O or CO_2.
2. The addition of water inhibits the catalytic methane conversion due to an increase in the OH(s) surface coverage that, in turn, reduces the available free Pt sites. The reduction of the catalytic reactivity with increasing water content can be significant at the large H_2O dilutions ($\sim 60\%$ vol.) of interest in new power generation cycles. The H_2O-induced heterogeneous inhibition is more pronounced at higher pressures and lower catalyst temperatures.
3. The water inhibition of the heterogeneous reactivity has been quantified with a global catalytic step having a power dependence of -0.36 on the water concentration. The global step provides methane conversions within 25% of those obtained with the detailed heterogeneous scheme.
4. The addition of CO_2 has no direct chemical impact on the catalytic pathway. Furthermore, the indirect impact of CO_2 addition through the dissociation of CO_2 to CO and the subsequent coupling of CO to the heterogeneous pathway is negligible at the temperatures of interest to practical catalytic combustion systems (< 1500 K).

5. The addition of water promotes chemically gaseous combustion and this effect is more pronounced at higher pressures and lower temperatures. The contribution of both catalytic and gas-phase pathways can be important for the determination of the total methane conversion at high pressures. High water dilutions accentuate the importance of the homogeneous pathway due to the resulting chemical promotion and inhibition of the gas-phase and catalytic reactivities, respectively. CO$_2$ has no chemical effect on the pre-ignition gas-phase chemistry at temperatures and equivalence ratios of interest to catalytic systems ($T < 1500$ K, $\varphi \leq 0.50$).

6. The impact of H$_2$O dilution on the hetero-/homogeneous radical coupling is weak. Even though large amounts of water dilution ($\sim 60\%$) can increase the OH desorption fluxes by an order of magnitude, their absolute magnitude is still too low to meaningfully affect the gas-phase chemistry over the induction zone.

NOMENCLATURE

b	channel half-height
c_p	specific heat at constant pressure
D_{km}	mixture-average diffusion coefficient of k-th gaseous species
D_k^T	thermal diffusion coefficient of k-th gaseous species
h	total enthalpy of gaseous mixture
h_k, h_k^o	total enthalpy and chemical enthalpy of k-th gaseous species
K_g	total number of gas-phase species
M_s	total number of surface species
p	pressure
R	universal gas constant
S	reactor surface
$\dot{s}_k$	heterogeneous molar production rate of k-th species
T	temperature
u, U_{IN}	streamwise velocity component, inlet streamwise velocity
v	transverse velocity component
$\vec{V}_k$	diffusion velocity vector of k-th gaseous species
V	reactor volume
$W_k, \overline{W}$	species molecular weight, average molecular weight
X_k, Y_k	gas-phase species mole and mass fraction
x, y, z	streamwise, transverse and lateral physical coordinates

Greek Symbols

Γ	surface site density
θ_m	surface species coverage
λ	thermal conductivity of gas
μ	viscosity
ρ	density
σ_m	surface species site occupancy
τ	reactor residence time
$\dot{\omega}_k$	gas-phase molar production rate of k-th species

Subscripts

ag	appreciable gas-phase conversion
ads	adsorption
des	desorption
IN	inlet
ig	ignition
k, m	indices for gas-phase and surface species
W	wall
x, y	streamwise and transverse components

Abbreviations

CST	Catalytically stabilized thermal combustion

REFERENCES

Aghalayam, P., Park, Y.K., Fernandes, N., Papavassiliou, V., Mhadeshwar, A.B., and Vlachos, D.G. (2003) A C1 mechanism for methane oxidation on platinum. *J. Catal.*, **213**, 23–38.

Appel, C., Mantzaras, J., Schaeren, R., Bombach, R., Inauen, A., Kaeppeli, B., Hemmerling, B., and Stampanoni, A. (2002) An experimental and numerical investigation of homogeneous ignition in catalytically stabilized combustion of hydrogen/air mixtures over platinum. *Combust. Flame*, **128**, 340–368.

Appel, C., Mantzaras, J., Schaeren, R., Bombach, R., and Inauen, A. (2005) Turbulent catalytically stabilized combustion of hydrogen/air mixtures in entry channel flows. *Combust. Flame*, **140**, 70–92.

Appel, C., Mantzaras, J., Schaeren, R., Bombach, R., Inauen, A., Tylli, N., Wolf, M., Griffin, T., Winkler, D., and Carroni, R. (2005a) Partial catalytic oxidation of methane to synthesis gas over rhodium: In situ Raman experiments and detailed simulations. *Proc. Combust. Instit.*, **30**, 2509–2517.

Beebe, K.W., Cairns, K.D., Pareek, V.K., Nickolas, S.G., Schlatter, J.C., and Tsuchiya, T. (2000) Development of catalytic combustion technology for single-digit emissions from industrial gas turbines. *Catal. Today*, **59**, 95–115.

Beer, S. and Willms, H. (1993) Control of an H$_2$/O$_2$ steam generator, Deutsches Zentrum für Luft- und Raumfahrt (DLR).

Brockhinke, A., Andresen, P., and Kohse-Höinghaus, K. (1995) Quantitative one-dimensional single-pulse multi-species concentration and temperature measurement in the lift-off region of a turbulent H$_2$/air diffusion flame. *Appl. Physics B*, **61**, 533–545.

Bui, P.A., Vlachos, D.G., and Westmoreland, P.R. (1996) Homogeneous ignition of hydrogen/air mixtures over platinum. *Proc. Combust. Instit.*, **26**, 1763–1770.

Carroni, R., Schmidt, V., and Griffin, T. (2002) Catalytic combustion for power generation. *Catal. Today*, **75**, 287–295.

Cattolica, R.J. and Schefer, R.W. (1983) Laser fluorescence measurements of the OH concentration in a combustion boundary layer. *Combust. Sci. Technol.*, **30**, 205–212.

Ciuparu, D. and Pfefferle, L.D. (2001) Support and water effects on palladium based methane combustion catalysts. *Appl. Catalysis A*, **209**, 415–428.

Coltrin, M.E., Kee, R.J., and Rupley, F.M. (1996) Surface Chemkin: A Fortran package for analyzing heterogeneous chemical kinetics at the solid surface-gas phase interface. Sandia National Laboratories, Report No. SAND90–8003C.

Deutschmann, O., Maier, L.I., Riedel, U., Stroemman, A.H., and Dibble, R.W. (2000) Hydrogen assisted catalytic combustion of methane on platinum. *Catal. Today*, **59**, 141–150.

Deutschmann, O., Schmidt, R., Behrendt, F., and Warnatz, J. (1996) Numerical modeling of catalytic ignition. *Proc. Combust. Instit.*, **26**, 1747–1754.

Dogwiler, U., Mantzaras, J., Benz, P., Kaeppeli, B., Bombach, R., and Arnold, A. (1998) Homogeneous ignition of methane/air mixtures over platinum: comparison of measurements and detailed numerical predictions. *Proc. Combust. Instit.*, **27**, 2275–2282.

Dogwiler, U., Benz, P., and Mantzaras, J. (1999) Two-dimensional modelling for catalytically stabilized combustion of a lean methane-air mixture with elementary homogeneous and heterogeneous chemical reactions. *Combust. Flame*, **116**, 243–258.

Eisenberg, S. (1995) *Raman Spectroscopy in a Jet Flame*, Diploma Thesis, Max-Planck-Institute for Fluid Mechanics, University of Goettingen.

Friedrichs, G., Herbon, J.T., Davidson, D.F., and Hanson, R.K. (2002) Quantitative detection of HCO behind shock waves: The thermal decomposition of HCO. *Phys. Chem. Chem. Phys.*, **4**, 5778–5788.

Gelin, P., Urfels, L., Primet, M., and Tena, E. (2003) Complete oxidation of methane at low temperature over Pt and Pd catalysts for the abatement of lean-burn natural gas fuelled vehicles emissions: Influence of water and sulphur containing compounds. *Catal. Today*, **83**, 45–57.

Griffin, T.A., Pfefferle, L.D., Dyer, M.J., and Crosley, D.R. (1989) The ignition of methane ethane boundary-layer flows by heated catalytic surface. *Combust. Sci. Technol.*, **65**, 19–37.

Griffin, T., Winkler, D., Wolf, M., Appel, C., and Mantzaras, J. (2004) Staged catalytic combustion method for the advanced zero emissions gas turbine power plant. ASME 2004–54101.

Groppi, G., Ibashi, W., Valentini, M., and Forzatti, P. (2001) High-temperature combustion of CH_4 over PdO/Al_2O_3: Kinetic measurements in a structured annular reactor. *Chem. Eng. Sci.*, **56**, 831–839.

Ibashi, W., Groppi, G., and Forzatti, P. (2003) Kinetic measurements of CH_4 combustion over a 10% PdO/ZrO_2 catalyst using an annular flow reactor. *Catal. Today*, **83**, 115–129.

Kee, R.J., Dixon-Lewis, G., Warnatz, J., Coltrin, M.E., and Miller, J.A. (1996) A Fortran computer code package for the evaluation of gas-phase multicomponent transport properties, Sandia National Laboratories, Report No. SAND86–8246.

Kee, R.J., Rupley, F.M., and Miller, J.A. (1996a) Chemkin II: A Fortran chemical kinetics package for the analysis of gas-phase chemical kinetics. Sandia National Laboratories, Report No. SAND89–8009B.

Kikuchi, R., Maeda, S., Sasaki, K., Wennerstroem, S., and Eguchi, K. (2002) Low-temperature methane oxidation over oxide-supported Pd catalysts: Inhibitory effect of water behavior. *Appl. Catal. A*, **232**, 23–28.

Liu, F., Guo, H., and Smallwood, G.J. (2003) The chemical effect of CO_2 replacement of N_2 in air on the burning velocity of CH_4 and H_2 premixed flames. *Combust. Flame*, **133**, 495–497.

Lutz, A.E., Kee, R.J., and Miller, J.A. (1996) SENKIN: A Fortran program for predicting homogeneous gas phase chemical kinetics with sensitivity analysis. Sandia National Laboratories, Report No. SAND87–8248.

Mantzaras, J., Appel, C., Benz, P. (2000a) Catalytic Combustion of Methane/Air Mixtures over Platinum: Homogeneous Ignition Distances in Channel Flow Configurations. *Proc. Combust. Instit.*, **28**, 1349–1357.

Mantzaras, J., Appel, C., Benz, P., and Dogwiler, U. (2000) Numerical modelling of turbulent catalytically stabilized channel flow combustion. *Catal. Today*, **53**, 3–17.

Mantzaras, J. and Appel, C. (2002) Effects of finite rate heterogeneous kinetics on homogeneous ignition in catalytically stabilized channel-flow combustion. *Combust. Flame*, **130**, 336–351.

Mantzaras, J. and Benz, P. (1999) An asymptotic and numerical investigation of homogeneous ignition in catalytically stabilized channel flow combustion. *Combust. Flame*, **119**, 455–472.

Moffat, H.K., Kee, R.J., Grcar, J.F., and Miller, J.A. (1993) Surface PSR: A Fortran program for modeling well-stirred reactors with gas and surface reactions. Sandia National Laboratories, Report No. SAND91–8001.

ONSE (1999) (Onsite Energy Corporation) Cost analysis of NO_x control alternatives for stationary gas turbines.

Patankar, S.V. (1980) Numerical Heat Transfer and Fluid Flow, Hemisphere Publ. Corp., New York.

Raja, L.L., Kee, R.J., Deutschmann, O., Warnatz, J., and Schmidt, L.D. (2000) A critical evaluation of Navier-Stokes, boundary-layer, and plug-flow models of the flow and chemistry in a catalytic-combustion monolith. *Catal. Today*, **59**, 47–60.

Reinke, M., Mantzaras, J., Schaeren, R., Bombach, R., Kreutner, W., and Inauen, A. (2002) Homogeneous Ignition in High-Pressure Combustion of Methane/Air over Platinum: Comparison of Measurements and Detailed Numerical Predictions. *Proc. Combust. Instit.*, **29**, 1021–1029.

Reinke, M., Mantzaras, J., Schaeren, R., Bombach, R., Inauen, A., and Schenker, S. (2004) High-pressure catalytic combustion of methane over platinum: In situ experiments and detailed numerical predictions. *Combust. Flame*, **136**, 217–240.

Reinke, M., Mantzaras, J., Bombach, R., Schenker, S., and Inauen, A. (2005) Gas phase chemistry in catalytic combustion of methane/air mixtures over platinum at pressures of 1 bar to 16 bar. *Combust. Flame*, **141**, 448–468.

Reinke, M., Mantzaras, J., Schaeren, R., Bombach, R., Inauen, A., and Schenker, S. (2005a) Homogeneous Ignition of CH_4/Air and H₂O- and CO₂-Diluted CH_4/O_2 Mixtures over Platinum; An Experimental and Numerical Investigation at Pressures up to 16 bar. *Proc. Combust. Instit.*, **30**, 2519–2527.

Schlegel, A., Benz, P., Griffin, T., Weisenstein, W., and Bockhorn, H. (1996) Catalytic stabilization of lean premixed combustion: Method for improving NO_x emissions. *Combust. Flame*, **105**, 332–340.

Sidwell, R.W., Zhu, H., Kee, R.J., Wickham, D.T., Schell, C., and Jackson, G.S. (2002) Catalytic Combustion of Premixed Methane-Air on a Palladium-Substituted Hexaaluminate Stagnation Surface. *Proc. Combust. Instit.*, **29**, 1013–1020.

Sidwell, R.W., Zhu, H., Kee, R.J., and Wickham, D.T. (2003) Catalytic combustion of premixed methane-in-air on a high-temperature hexaaluminate stagnation surface. *Combust. Flame*, **134**, 55–66.

Snow, G.C., Krill, W.V., Chu, E.K., and Kendall, R.K. (1984) Mechanisms and kinetics in catalytic combustion. Report No. EPA-600/9-84-002.

Steiner, B. (2002) Raman spectroscopic investigation of turbulent premixed flames, Ph.D. Thesis, University of Stuttgart.

Taylor, J.D., Allendorf, M.D., Mc Daniel, A.H., and Rice, S.F. (2003) In situ diagnostics and modeling of methane catalytic partial oxidation on Pt in a stagnation-flow reactor. *Ind. Eng. Chem. Res.*, **42**, 6559–6566.

Urfels, L., Gelin, P., Primet, M., and Tena, E. (2004) Complete oxidation of methane at low temperature over Pt catalysts supported on high surface area SnO_2. *Topics Catal.*, **30–31**, 427–432.

van Giezen, J.C., van den Berg, F.R., Kleinen, J.L., van Dillen, A.J., and Geus, J.W. (1999) The effect of water on the activity of supported palladium catalysts in the catalytic combustion of methane. *Catal. Today*, **47**, 287–293.

Warnatz, J., Allendorf, M.D., Kee, R.J., and Coltrin, M.E. (1994) A model of elementary chemistry and fluid mechanics in the combustion of hydrogen on platinum surfaces. *Combust. Flame*, **96**, 393–406.

Warnatz, J., Dibble, R.W., and Maas, U. (1996) Combustion, Physical and Chemical Fundamentals, Modeling and Simulation, Springer-Verlag, New York. Mechanism also available at: ⟨http://reaflow.iwr.uni-heidelberg.de/∼ ftp/ reaflow/mechanism_for_export/Mech97.C1_C2_incl_thermodynamics⟩

Westbrook, C.K. and Dryer, F.L. (1981) Simplified reaction mechanisms for the oxidation of hydrocarbon fuels in flames. *Combust. Sci. Technol.*, **27**, 31–43.

Zerkle, D.K., Allendorf, M.D., Wolf, M., and Deutschmann, O. (2000) Understanding homogeneous and heterogeneous contributions to the platinum-catalyzed partial oxidation of ethane in a short-contact-time reactor. *J. Catal.*, **196**, 18–39.